THE ASTROPHYSICAL JOURNAL, 220:1001–1023, 1978 March 15

TWO-DIMENSIONAL RADIATIVE TRANSFER. I. PLANAR GEOMETRY

DIMITRI MIHALAS AND L. H. AUER
High Altitude Observatory, National Center for Atmospheric Research*
AND
BARBARA R. MIHALAS
Department of Astrogeophysics, University of Colorado
Received 1977 August 15; accepted 1977 September 15

ABSTRACT

Differential-equation methods for solving the transfer equation in two-dimensional planar geometries are developed. One method, which uses a Hermitian integration formula on ray segments through grid points, proves to be extremely well suited to velocity-dependent problems. An efficient elimination scheme is developed for which the computing time scales *linearly* with the number of angles and frequencies; we are thus able to treat problems with large velocity amplitudes accurately.

A very accurate and efficient method for performing a formal solution is also presented. A discussion is given of several examples of periodic media and freestanding slabs, both in static cases and with velocity fields. For the freestanding slabs, two-dimensional transport effects are significant near boundaries, but no important effects were found in any of the periodic cases that we have studied.

Subject headings: radiative transfer — stars: atmospheres

I. INTRODUCTION

When the solar atmosphere is observed with high spatial, temporal, and wavelength resolution, an enormous variety of small-scale structural features is found. These features indicate the presence of strong local variations in the basic physical properties of the atmospheric material, and are often associated with velocity and magnetic fields. The interpretation of spectral lines observed in these structures offers the opportunity of obtaining insight into their origin, dynamical behavior, evolution, and effect upon the atmosphere. However, as many of the observed structures are of very small size, there can be significant radiative interaction with neighboring regions having different physical properties; and before we can believe our diagnostics, we must fully understand the effects of lateral transport upon the observed spectrum. In addition, one can observe essentially isolated structures (both *freestanding* such as prominences, or *embedded* in an ambient medium, such as sunspots or the supergranulation network). These are strongly influenced by the basic geometric configuration and by externally imposed boundary conditions (i.e., incident radiation fields). A fully satisfactory analysis of them must be based on a detailed spectroscopic study in which full allowance is made for the multidimensional physical structure and for the presence of complicated velocity fields.

Considerable effort has been expended by a number of astronomers on the solution of multidimensional transfer problems. This work ranges from computations of emergent spectra from multidimensional (or multicomponent) media in which the source function is presumed to be *known* (i.e., a *formal solution*) to full solutions of the coupled transfer and statistical equilibrium equations. A wide variety of mathematical techniques has been employed, including integration along rays, differential equation methods, integral equation methods, and Fourier transform techniques. As an extensive review of the physical effects of multidimensional radiative transfer (Jones and Skumanich 1977) and an exhaustive bibliography of the relevant literature (Cram, Durrant, and Kneer 1977) have recently appeared, we shall not attempt such a summary here. A concise statement of the present status of the field can be reduced to the following remarks: while substantial progress has been made toward the solution of multidimensional problems, no one approach has yet solved the full range of problems satisfactorily, and further development of mathematical methods is needed.

In this paper we describe effective methods for solving the transfer problems for two-level atoms in two-dimensional planar media (with velocity fields). The published work most closely related to ours is that of Cannon (1970) and Cannon and Rees (1971).

The principal new features in the present approach are as follows: (1) In addition to ordinary difference-equation methods, we have developed a hybrid scheme that incorporates the best features of ray-tracing methods (by solving the transfer problem along a characteristic ray) and difference-equation methods (by centering the rays onto a

* The National Center for Atmospheric Research is sponsored by the National Science Foundation.

regular rectangular mesh) and uses a high-order Hermitian integration formula (Auer 1976). In practice this new approach is superior to difference-equation techniques, especially when there are velocity fields present. In fact, it provides solutions with ease in cases where the standard difference equations fail totally. (2) We employ an elimination scheme related to that developed by Rybicki (1971) for one-dimensional problems; as a result the computing time is only *linear* in the number of angles and frequencies used in the quadrature formulae for the scattering integral. Such a scaling is very favorable when velocity fields are present. (3) An efficient and accurate method is employed in the formal solution, i.e., in the calculation of the emergent intensity as a function of position, angle, and frequency for a given source function. (4) We have treated a wide range of boundary conditions, including those applicable to *periodic* media, structures *embedded* in ambient atmospheres, and *freestanding* structures.

Our presentation will be basically methodological, and the applications described in § III are meant to be only *illustrative*, and are *not* attempts to model real structures in the actual solar atmosphere (though reasonable values for most parameters have been chosen). The computer programs that implement our technique are available to interested investigators as part of the High Altitude Observatory Radiative Transfer Library, and we hope that they will be extensively used.

II. METHOD

a) Differential Equations and Boundary Conditions

Consider a region $(0 \leq x \leq X)$, $(-Z \leq z \leq 0)$ in the (x, z)-plane, as shown in Figure 1, representing a cross section of the atmosphere over which material properties and radiation fields vary; the medium is assumed to be infinite and strictly homogeneous in the y-direction, which is perpendicular to the plane shown. We shall refer to the surface $(x, 0)$ as the "top" of the atmosphere, the surface $(x, -Z)$ as the "bottom" of the atmosphere, the surface $(0, z)$ as the "left-hand" boundary, and the surface (X, z) as the "right-hand" boundary. Now consider a ray along which radiation propagates at angle θ to the z-axis, and whose projection on the (x, y)-plane is at an angle ϕ to the x-axis; let $\mu = \cos\theta$ and $\gamma = \sin\theta\cos\phi$. Then the transfer equation along the ray is

$$\frac{\mu}{\chi}\frac{\partial I}{\partial z} + \frac{\gamma}{\chi}\frac{\partial I}{\partial x} = S - I\,, \tag{1}$$

where $I = I(x, z, \nu, \theta, \phi)$, and the opacity is

$$\chi(x, z, \nu, \theta, \phi) = \chi_L(x, z)\Phi(x, z, \nu, \theta, \phi) + \chi_c(x, z) \equiv \chi_c(x, z)[1 + \beta(x, z)\Phi]\,. \tag{2}$$

Here χ_L and χ_c denote the line and continuum opacity respectively, and Φ is the line profile function. For definiteness we shall use a Doppler profile throughout this paper and we shall measure frequencies and velocities in terms of a fiducial Doppler width $\Delta\nu_D$*. Then

$$\Phi(x, z, \nu, \theta, \phi) = \pi^{-1/2}\Delta(x, z)\exp\{-\Delta(x, z)^2[\nu - \mu v_z(x, z) - \gamma v_x(x, z)]^2\}\,, \tag{3}$$

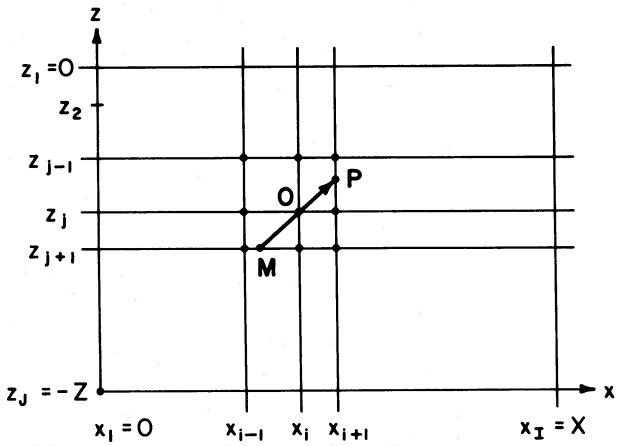

FIG. 1.—Geometry of planar slab. The medium is assumed to be infinite and homogeneous in the y-direction (out of the plane of the figure). Indexing conventions are described in the text.

where $\Delta(x, z) \equiv \Delta\nu_D^*/\Delta\nu_D(x, z)$ is the reciprocal Doppler width in fiducial units. Generalization to any other profile function offers no difficulty. The source function is taken to be that appropriate to a two-level atom with complete redistribution, i.e.,

$$S(x, z, \nu, \theta, \phi) = \frac{[1 - \epsilon(x, z)]\beta(x, z)\Phi(x, z, \nu, \theta, \phi)}{1 + \beta(x, z)\Phi(x, z, \nu, \theta, \phi)} \int d\nu \oint \frac{d\omega}{4\pi} I(x, z, \nu, \theta, \phi)\Phi(x, z, \nu, \theta, \phi)$$

$$+ \frac{[1 + \epsilon(x, z)\beta(x, z)\Phi(x, z, \nu, \theta, \phi)]}{1 + \beta(x, z)\Phi(x, z, \nu, \theta, \phi)} B(x, z)$$

$$\equiv [1 - \xi(x, z, \nu, \theta, \phi)]\bar{J}(x, z) + \xi(x, z, \nu, \theta, \phi)B(x, z) . \quad (4)$$

Here ξ measures the total destruction probability of a photon, B denotes an equivalent thermal source term (which may in principle include photoionization-recombination terms), and ϵ is the collisional destruction probability $\epsilon = C_{ul}/(P_{ul} + C_{ul})$.

The assumption of complete redistribution is more restrictive than that made by Cannon (1970) and Cannon and Rees (1971), whose method can treat partial redistribution. However, this restriction offers the major advantage that we can employ the Rybicki (1971) elimination scheme with a considerable gain in computational economy compared to the Feautrier (1964) scheme when large numbers of angles and frequencies are required to evaluate the scattering integral. Given the primitive state of our insight into multidimensional transfer problems, we feel that it is worthwhile to sacrifice the refinement of partial redistribution in favor of low computation cost.

The transfer equation may be cast into second-order form by use of the symmetric and antisymmetric averages for the specific intensity along a ray, namely,

$$u = u(x, z, \nu, \mu, \gamma) \equiv \tfrac{1}{2}[I(x, z, \nu, \mu, \gamma) + I(x, z, -\nu, -\mu, -\gamma)] \quad (5a)$$

and

$$v = v(x, z, \nu, \mu, \gamma) \equiv \tfrac{1}{2}[I(x, z, \nu, \mu, \gamma) - I(x, z, -\nu, -\mu, -\gamma)] . \quad (5b)$$

Having assumed that the medium is homogeneous in the y-direction, we shall take both the internal radiation field and the imposed boundary conditions to be symmetric with respect to the (x, z)-plane. Thus to describe the radiation field in the most general case we must consider the ranges $0 \leq \mu \leq 1$, $-1 \leq \gamma \leq 1$. In the event that the physical properties in the slab are symmetric about the midpoint $X/2$ [except for $v_x(x, z)$ which is *antisymmetric*], and the radiation fields imposed on the left-hand and right-hand boundaries are the same, then we need to consider only $0 \leq \mu \leq 1$ and $0 \leq \gamma \leq 1$, for then $u(x, z, \nu, \mu, -\gamma) \equiv u(X - x, z, \nu, \mu, \gamma)$. We must, however, still consider the full range $0 \leq x \leq X$.

Writing equation (1) in terms of u and v, we have

$$\frac{\mu}{\chi}\frac{\partial u}{\partial z} + \frac{\gamma}{\chi}\frac{\partial u}{\partial x} = -v \quad (6a)$$

and

$$\frac{\mu}{\chi}\frac{\partial v}{\partial z} + \frac{\gamma}{\chi}\frac{\partial v}{\partial x} = S - u ; \quad (6b)$$

or substituting for v from (6a) into (6b) we have

$$\left(\frac{\mu}{\chi}\frac{\partial}{\partial z} + \frac{\gamma}{\chi}\frac{\partial}{\partial x}\right)^2 u = u - S . \quad (7)$$

Boundary conditions on each face follow directly from equations (5) and (6a). They are always of the form

$$\frac{\mu}{\chi}\frac{\partial u}{\partial z} + \frac{\gamma}{\chi}\frac{\partial u}{\partial x} = au + b . \quad (8)$$

b) Discretization

We now introduce discretizations in space, angle, and frequency in order to reduce the partial differential equations to a set of linear algebraic equations. We choose a spatial mesh $\{x_i, z_j\}$ $(i = 1, \ldots, I; j = 1, \ldots, J)$ spanning the domain (see Fig. 1). For atmospheres in which the density (and hence opacity) rises exponentially with depth it is advantageous to use uniform steps in Δz, as this yields a logarithmic spacing in optical depth along z. For media with almost constant properties a logarithmic spacing in x and z is preferable (see Fig. 2).

To describe the angular dependence of the radiation field we used the rotation-invariant discrete mesh $\{u_l, \gamma_l\}$ $(l = 1, \ldots, L)$ of Carlson (1963). The majority of the results reported here were computed with his "Set B" with

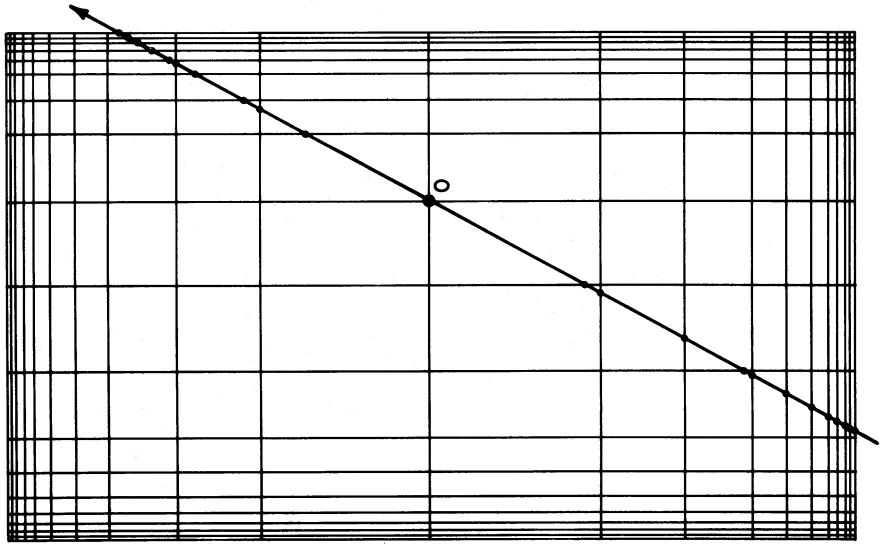

FIG. 2.—Mesh-lines for a finite slab with logarithmic spacing of the intervals away from the boundary surfaces; such a choice is appropriate in, e.g., a homogeneous freestanding slab. Note that the ray through the grid-point O does not, in general, intersect any of the other grid-points defined by the intersections of mesh lines, and, further, that the spacing of points of intersection of the ray with the mesh lines is extremely irregular.

six points per octant. Our "Eddington approximation" results correspond to the choices $L = 1$, $\mu_1 = \gamma_1 = 1/\sqrt{3}$, which implies $\theta = \cos^{-1}(1/\sqrt{3})$ and $\phi = \pi/4$.

For the frequency quadrature we have used the trapezoidal rule with equal steps of $0.5\Delta\nu_D^*$. If the frequency mesh (measured in units of $\Delta\nu_D^*$) is $\{\nu_f\}$ $(f = 1, \ldots, F)$, then the scattering integral is approximated by the expression

$$\bar{J}_{ij} \equiv \bar{J}(x_i, z_j) = \pi^{-3/2}\Delta_{ij}\int_{-\infty}^{\infty} d\nu \int_0^{\pi} d\phi \int_0^1 d\mu \exp\left[-\Delta_{ij}^2(\nu - \mu v_z - \gamma v_x)^2\right] u(x_i, z_j, \mu, \gamma, \nu) \approx \sum_{k=1}^{K} w_k \Phi_{ijk} u_{ijk} . \quad (9)$$

Here the angle and frequency quadratures have been combined into a single product quadrature with $K = L \cdot F$.

c) *Approximation of the Differential Operator*

Discrete representations of the differential operator in equation (7) can be developed from two different points of view. One approach is to use an ordinary difference-equation approximation as described in Appendix A; this, however, proves unsatisfactory when velocity fields are present. Alternatively, we observe that the differential operator in equation (7) is simply the second derivative with respect to the optical path-length *along the ray* (which is a characteristic of the equation). Thus choosing $\tau_{\nu\mu\gamma}$, the optical depth along the ray, as an independent variable we can reduce the partial differential equation for the two-dimensional problem to an equivalent one-dimensional problem described by the ordinary differential equation

$$\frac{d^2 u_{\nu\mu\gamma}}{d\tau_{\nu\mu\gamma}^2} = u_{\nu\mu\gamma} - S_{\nu\mu\gamma} . \quad (10)$$

To solve this equation we can apply a high-order Hermitian formula (Auer 1976) which is very accurate and stable.

If we were always able to use the Eddington approximation with $\Delta x = \Delta z =$ constant, the integration procedure would be simple because in this case each ray goes through only grid-points, and no interpolation is necessary. Unfortunately, this is not the usual situation (cf. Fig. 2), for in general a ray through a particular grid-point will not pass through any other grid-point, and, in addition, the spacing of the points of intersection of the ray with the prechosen mesh-lines is very irregular. Thus a more elaborate method must be employed. If one attempts to perform the integration literally along a ray passing entirely through the medium from one boundary surface to another, the interpolation problems encountered are severe (Jones and Skumanich 1973; Jones 1973). But these difficulties can be overcome elegantly by integrating along a ray through *each* grid-point *only* from that point to the point of intersection of the ray with the *next* mesh-line. The procedure is illustrated in Figure 1, where the integration extends only from M through O to P. Values of the physical variables and the radiation field at points M and P are obtained by parabolic interpolation on the periphery of the nine-point stencil surrounding point O.

The requisite interpolations can be carried out with high accuracy because they occur along mesh-lines. This approach is similar to an idea used by Hartree (Hartree 1958; Fox 1962) for the solution of partial differential equations along curved characteristics.

Consider Figure 1; let $\Delta\tau_+$ and $\Delta\tau_-$ be the optical-depth increments from M to O and from O to P, respectively. Then the Hermite formula (suppressing unnecessary subscripts) is

$$-(a - A)u_M + (1 + a + c - A - C)u_O - (c - C)u_P = AS_M + (1 - A - C)S_O + CS_P , \tag{11}$$

where

$$a \equiv 2/[\Delta\tau_-(\Delta\tau_- + \Delta\tau_+)] , \tag{12a}$$

$$c \equiv 2/[\Delta\tau_+(\Delta\tau_- + \Delta\tau_+)] , \tag{12b}$$

$$A \equiv \tfrac{1}{6}(1 - \tfrac{1}{2}a\Delta\tau_+^2) , \tag{12c}$$

and

$$C \equiv \tfrac{1}{6}(1 - \tfrac{1}{2}c\Delta\tau_-^2) . \tag{12d}$$

As noted above, points M and P are in general not grid points, and physical quantities at these points are obtained by interpolation. If O is at (i, j) in the grid, then after substituting the interpolation formula, equation (11) reduces at interior points to the general form

$$\sum_{j'=j-1}^{j+1} \sum_{i'=i-1}^{i+1} (k_{i'j'}u_{i'j'} + l_{i'j'}\bar{J}_{i'j'}) = m_{ij} . \tag{13}$$

Equations that apply at boundary points are derived from equation (8) by similar considerations. If O is a grid-point on an exterior boundary, we have a third-order equation of the form

$$u_P\left(\frac{1}{\Delta\tau} - \tfrac{1}{6}\Delta\tau\right) - u_O\left(\frac{1}{\Delta\tau} + \tfrac{1}{3}\Delta\tau + a\right) = b - \tfrac{1}{6}\Delta\tau(2S_O + S_P) . \tag{14}$$

Again the necessary values at P are expressed in terms of grid values by means of Lagrangian interpolation. At periodic boundaries equation (13) applies directly with suitable relabeling of grid-points across the interface.

Because quantities such as $\bar{J}$, $\ln \chi_c$, v_x, v_z, Δ, ϵ, β, and B are relatively slowly varying functions of position, they can be interpolated directly. For the profile function Φ it is essential in the presence of velocity field to interpolate not Φ itself, but the variables determining the value of its argument (i.e., Δ, v_x, and v_z), and then to compute Φ_M or Φ_P explicitly. The method used to evaluate the optical depth increments is described in Appendix B.

In practice the Hermitian ray-integration and the difference-equation methods work about equally well for *static* media. But for cases with velocity fields of sizable amplitudes the Hermitian method is overwhelmingly superior. In these cases the difference equations often fail and yield negative radiation fields or singular systems of equations; the problem is that differencing $\Delta\tau$ along the mesh-lines gives a poor representation of its behavior along a ray. In contrast, the Hermitian method treats directly the opacity variation along the actual ray on which the radiation propagates, and thus retains excellent accuracy and stability.

Finally, it should be noted that both schemes are *automatically* consistent with the diffusion approximation at great depth; this is not the case with some other methods (e.g., integral-equation methods) where special efforts must be made to secure this consistency.

d) Elimination Scheme

For a given choice of the angle-frequency index k, we organize the x-variation of u_{ijk} at a specific depth z_j into a vector

$$\boldsymbol{u}_j \equiv (u_{1j}, u_{2j}, \ldots, u_{Ij})^T \tag{15}$$

(the subscript k is suppressed here and through eq. [26] for brevity). Then the transfer equation, including boundary conditions, can be written in the general form

$$\boldsymbol{A}_j\boldsymbol{u}_{j-1} + \boldsymbol{B}_j\boldsymbol{u}_j + \boldsymbol{C}_j\boldsymbol{u}_{j+1} = \sum_{j'=j-1}^{j+1} \boldsymbol{D}_{jj'}\bar{\boldsymbol{J}}_{j'} + \boldsymbol{E}_j , \tag{16}$$

where

$$\bar{\boldsymbol{J}}_j \equiv (\bar{J}_{1j}, \bar{J}_{2j}, \ldots, \bar{J}_{Ij})^T , \tag{17}$$

The matrices $\boldsymbol{A}$, $\boldsymbol{B}$, and $\boldsymbol{C}$ are of dimension $(I \times I)$ and are tridiagonal or periodic tridiagonal. For nonsymmetric cases the $\boldsymbol{D}$ matrices are of dimension $(I \times I)$. If the medium is *symmetric* about a midpoint whose index is I_m, then we need consider only the range $i = 1, \ldots, I_m$ for $\bar{J}_{ij}$ and the $\boldsymbol{D}$ matrices become $(I \times I_m)$ chevron matrices.

Equations (16) for $(j = 1, \ldots, J)$ can be solved by a forward-elimination, back-substitution scheme. The recursion formula for the forward elimination is easily shown to be of the form

$$\boldsymbol{u}_j = -\boldsymbol{U}_j \boldsymbol{u}_{j+1} + \sum_{j' \le j+1} \boldsymbol{V}_{jj'} \bar{\boldsymbol{J}}_{j'} + \boldsymbol{W}_j , \tag{18}$$

where

$$\boldsymbol{W}_j \equiv (\boldsymbol{B}_j - \boldsymbol{A}_j \boldsymbol{U}_{j-1})^{-1} (\boldsymbol{E}_j - \boldsymbol{A}_j \boldsymbol{W}_{j-1}) , \tag{19}$$

$$\boldsymbol{U}_j \equiv (\boldsymbol{B}_j - \boldsymbol{A}_j \boldsymbol{U}_{j-1})^{-1} \boldsymbol{C}_j , \tag{20}$$

$$\boldsymbol{V}_{j,j+1} \equiv (\boldsymbol{B}_j - \boldsymbol{A}_j \boldsymbol{U}_{j-1})^{-1} \boldsymbol{D}_{j,j+1} , \tag{21a}$$

$$\boldsymbol{V}_{jj'} \equiv (\boldsymbol{B}_j - \boldsymbol{A}_j \boldsymbol{U}_{j-1})^{-1} (\boldsymbol{D}_{jj'} - \boldsymbol{A}_j \boldsymbol{V}_{j-1,j'}) \quad (j' = j, j-1) , \tag{21b}$$

and

$$\boldsymbol{V}_{jj'} = -(\boldsymbol{B}_j - \boldsymbol{A}_j \boldsymbol{U}_{j-1})^{-1} \boldsymbol{A}_j \boldsymbol{V}_{j-1,j'} \quad (j' < j-1) . \tag{21c}$$

The matrices $\boldsymbol{U}$ and $\boldsymbol{V}$ are full, and in the general case are of dimension $(I \times I)$; for a symmetric medium the $\boldsymbol{V}$ matrices collapse to dimension $(I \times I_m)$. The boundary conditions imply that $\boldsymbol{A}_1 \equiv 0$, $\boldsymbol{D}_{10} \equiv 0$, $\boldsymbol{C}_j \equiv 0$, and $\boldsymbol{D}_{J,J+1} \equiv 0$; thus the forward elimination can be carried out straightaway to obtain all $\boldsymbol{U}_j$ and $\boldsymbol{V}_{jj'}$ matrices for $j = 1, \ldots, J$.

Having completed the forward elimination, we can now back-substitute to develop relations of the form

$$\boldsymbol{u}_j = \sum_{j'=1}^{J} \boldsymbol{X}_{jj'} \bar{\boldsymbol{J}}_{j'} + \boldsymbol{Y}_j , \tag{22}$$

where for $j = J$

$$\boldsymbol{X}_{Jj'} = \boldsymbol{V}_{Jj'} \quad \text{and} \quad \boldsymbol{Y}_J = \boldsymbol{W}_J ; \tag{23), (24}$$

and for $j < J$

$$\boldsymbol{X}_{jj'} = \boldsymbol{V}_{jj'} - \boldsymbol{U}_j \boldsymbol{X}_{j+1,j'} \quad (j' \le j+1) , \tag{25a}$$

$$\boldsymbol{X}_{jj'} = -\boldsymbol{U}_j \boldsymbol{X}_{j+1,j'} \quad (j' > j+1) , \tag{25b}$$

$$\boldsymbol{Y}_j = \boldsymbol{W}_j - \boldsymbol{U}_j \boldsymbol{Y}_{j+1} . \tag{26}$$

The $\boldsymbol{X}$ matrices are of dimension $(I \times I)$ in the general case and $(I \times I_M)$ for the symmetric case; the vectors $\boldsymbol{Y}$ are of dimension I. The back-substitution is carried out for $j = J, \ldots, 2, 1$ using equations (23)–(26).

The whole forward-elimination, back-substitution scheme is carried out for each of the K angle-frequency choices, and the results used in equation (9), which may be written as

$$\bar{\boldsymbol{J}}_j = \sum_{k=1}^{K} \boldsymbol{F}_{jk} \boldsymbol{u}_{jk} , \tag{27}$$

to develop, ultimately, the linear system

$$\bar{\boldsymbol{J}}_j = \sum_{j'=1}^{J} \boldsymbol{G}_{jj'} \bar{\boldsymbol{J}}_{j'} + \boldsymbol{H}_j \quad (j = 1, \ldots, J) , \tag{28}$$

where

$$\boldsymbol{G}_{jj'} \equiv \sum_{k=1}^{K} \boldsymbol{F}_{jk} \boldsymbol{X}_{jj',k} \tag{29}$$

and

$$\boldsymbol{H}_j \equiv \sum_{k=1}^{K} \boldsymbol{F}_{jk} \boldsymbol{Y}_{jk} . \tag{30}$$

Solution of the system (28) yields the full spatial variation of $\bar{J}(x, z)$, from which the spatial and frequency dependence of the source function can be computed via equation (4). The weight matrices in the general case are diagonal and are of dimension I; in the symmetric case they are $(I_m \times I)$ chevron matrices. In the general case the $\boldsymbol{G}$ matrices are of dimension $(I \times I)$, but for symmetric media they are of dimension $(I_m \times I_m)$. In the general case final system (28) is of dimension $(IJ \times IJ)$; in the symmetric case it is of dimension $(I_m J \times I_m J)$.

The forward-elimination back-substitution scheme requires of the order of $(3/2)KI^3J^2$ or $(3/2)KI_m{}^3J^2$ multiplications in the general and symmetric cases, respectively. We have solved the final system (28) *directly*, which requires on the order of $\frac{1}{3}I^3J^3$ or $\frac{1}{3}I_m{}^3J^3$ multiplications; it would also be possible to employ an iterative method

(e.g., a block successive overrelaxation scheme), but in practice the final system solution requires much less time than the forward-elimination, back-substitution procedure, so little if any economy would be realized. The overall scaling of the computing time is $T \sim I^3J^2(c_1K + c_2J)$ or $T \sim I_mJ^2(c_1'I^2K + c_2'I_m^2J)$ for the general and symmetric cases, respectively; the first terms in the parentheses dominate.

The number of multiplications required by Cannon's method (1970) is of the order of K^3I^3J, so that the computing times for the two schemes are in the ratio (Cannon/present) $\sim K^2/J$. Thus the present method becomes quite favorable when the number of angle-frequency points must be large. For two reasons, the number K becomes large when velocity fields of several Doppler widths occur. First, a sufficient number of frequencies must be chosen to cover the full profile plus Doppler shift, i.e., a range of about $\pm(3.5 + |V|_{\max})$ Doppler units (typically in steps of $\frac{1}{2}$ Doppler unit). Second, if a frequency step $\Delta x = \Delta\nu/\Delta\nu_D{}^*$ is selected to provide a certain level of accuracy for the frequency quadrature in equation (9), then angles must be chosen so that $|\Delta\mu|$ (or $|\Delta\gamma|$) $\lesssim \Delta x/|V|_{\max}$ to retain this accuracy. If $|V|_{\max} \sim 2$ (as in cases we have considered below) and $\Delta x \sim \frac{1}{2}$, clearly *several* angles per octant are indicated. We have treated cases with as many as 12 angles per octant and 23 frequencies in the line without prohibitive cost; such cases would be essentially intractable with Cannon's method.

Finally, it should be noted that although the method has been described for a two-level atom problem, it can, in principle, be generalized to treat multilevel atoms, at least using the equivalent-two-level-atom (ETLA) approach. In such a scheme one would solve for $\bar{J}$ in each of several transitions, one at a time, in turn, and use the resulting source functions and $\bar{J}$'s to evaluate rates (or net rates) required by the analytical ETLA source function expressions. One then would attempt to iterate all of the radiation fields to self-consistency. In practice such a calculation would be quite costly, and there is much yet to be learned even from strict two-level-atom calculations before a multilevel computation will be worthwhile.

e) Formal Solution for Emergent Intensities

Having obtained the (x, z) variation of the source function, we are finally in a position to calculate the observable emergent intensity as a function of frequency, angle, and position on some chosen boundary of the medium. This is, of course, precisely the information needed to diagnose conditions in the material, and to predict line shapes and strengths for a given model.

The problem of calculating the emergent radiation field from the formal solution of the transfer equation reduces to the quadrature

$$I(x_0, z_0) = \int_0^{\tau_{\max}} S(x, z)e^{-\tau(x,z)}d\tau(x, z) + I_{\rm BC}\exp(-\tau_{\max})\,. \tag{31}$$

Here (x_0, z_0) denotes the position at which the ray exits from the medium. The optical depth $\tau(x, z)$ is measured *along the ray*, whose path length is s, i.e., $\tau(x, z) = \int \chi[x'(s), z'(s)]ds$, where $x'(s) = x_0 - s/\gamma$, and $z'(s) = z_0 - s/|\mu|$. Also, $I_{\rm BC}$ is the incident intensity at the relevant boundary where the ray first penetrates into the medium.

Because $S(x, z)$ is known only at a discrete set of grid points, we cannot perform the integration indicated in equation (31) directly. Instead, we break the integral into a sum over discrete intervals spanning the range between successive intersections of the ray with the boundaries of the cells defined by the mesh lines (cf. Fig. 2). Thus

$$\int_0^{\tau_{\max}} Se^{-\tau}d\tau = \sum_{k=1}^{N-1}\int_{\tau_k}^{\tau_{k+1}} Se^{-\tau}d\tau\,, \tag{32}$$

where $\tau_1 = 0$ and $\tau_N = \tau_{\max}$. Hence the problem is reduced to that of finding an appropriate approximation to $\int Se^{-\tau}d\tau$ on (τ_k, τ_{k+1}), the contributions from a single cell.

In performing the ray integration we can recognize two severe difficulties that arise in the multidimensional case and that are not present in the one-dimensional case. First, the spacing of the intervals along the ray may be highly irregular, as illustrated in Figure 2. There is no way in which the (x, z) grid can be chosen to avoid this problem for all angles and positions. Second, we must interpolate for S and χ. In general a ray enters and leaves a cell by cutting through a mesh line defining the edge of the cell, rather than by passing through a grid point. We know the source function, however, only on the grid. The interpolation problem is particularly difficult because all interpolation must be done in the physical variables x and z, as it is practical to interpolate only on a Cartesian grid. Unfortunately, the large-scale variation of S is likely to be badly represented by polynomials in x and z. To see why this is so, we note that in the one-dimensional case S can often be approximated by a linear function of $\tau = -\int \chi dz$; but in a stellar atmosphere in hydrostatic equilibrium $\chi \propto \exp(-\alpha z)$ (recall $z < 0$). Thus the variation of S is, in general, more nearly *exponential* in x and z, and this variation will be poorly approximated by polynomials in these variables except over very small intervals.

i) *Integration Formula*

The first difficulty mentioned above implies that we require an accurate, stable, high-order method for the computation of the integral $\int Se^{-\tau}d\tau$ between the limits $[\tau_k, \tau_{k+1}]$. The method we employ meets these criteria,

and is exact if S can be represented by a cubic in τ on the discrete interval. Indeed we implicitly represent S as a piecewise cubic in τ over the entire length of the ray. On each subinterval we approximate S by a distinct cubic Hermite interpolating polynomial in τ. Thus if S_0 and S_1 are the values of the source function at τ_0 and τ_1, and S_0' and S_1' are the corresponding first derivatives with respect to τ, the approximating Hermite polynomial on (τ_0, τ_1) is

$$S(\tau) = S_0(1 - 3\xi^2 + 2\xi^3) + S_1(3\xi^2 - 2\xi^3) + \Delta\tau[S_0'(\xi - 2\xi^2 + \xi^3) + S_1'(-\xi^2 + \xi^3)]\,. \tag{33}$$

Here $\Delta\tau \equiv \tau_1 - \tau_0$, and $\xi \equiv (\tau - \tau_0)/\Delta\tau$. To avoid roundoff problems we may write the equivalent expansion

$$S(\tau) = \tilde{S} + \tilde{S}'\rho + \tfrac{1}{2}\tilde{S}''\rho^2 + \tfrac{1}{6}\tilde{S}'''\rho^3\,, \tag{34}$$

where $\rho \equiv \tau - \frac{1}{2}(\tau_0 + \tau_1)$. The coefficients $\tilde{S}$, $\tilde{S}'$, etc., are clearly approximations to S and its derivative at the midpoint of the interval. They are found to be

$$\tilde{S} = \tfrac{1}{2}(S_0 + S_1) - \tfrac{1}{8}(S_1' - S_0')\Delta\tau\,, \tag{35a}$$

$$\tilde{S}' = \tfrac{3}{2}(S_1 - S_0)/\Delta\tau - \tfrac{1}{4}(S_1' + S_0')\,, \tag{35b}$$

$$\tilde{S}'' = (S_1' - S_0')/\Delta\tau\,, \tag{35c}$$

$$\tilde{S}''' = 6[(S_1' + S_0')\Delta\tau - 2(S_1 - S_0)]/\Delta\tau^3. \tag{35d}$$

Substituting equations (34)–(35d) into the integral, we find the desired quadrature formula:

$$\int_{\tau_0}^{\tau_1} S(\tau)e^{-\tau}d\tau \approx e^{-\tau_0}(\omega\tilde{S} + \omega'\tilde{S}' + \omega''\tilde{S}'' + \omega'''\tilde{S}''')\,. \tag{36}$$

For $\Delta\tau \gtrsim 1$, the weights may be found by upward recursion,

$$\omega = 1 - e^{-\Delta\tau}\,, \tag{37a}$$

$$\omega' = \omega - \tfrac{1}{2}\Delta\tau(1 + e^{-\Delta\tau})\,, \tag{37b}$$

$$\omega'' = \omega' + \tfrac{1}{8}\Delta\tau^2\omega\,, \tag{37c}$$

$$\omega''' = \omega'' - \Delta\tau^3(1 + e^{-\Delta\tau})/48\,. \tag{37d}$$

For $\Delta\tau \leq 1$, the recursion is done downward starting from

$$\omega''' = -\tfrac{1}{3}e^{-\Delta\tau/2}\left[\frac{1}{5}\left(\frac{\Delta\tau}{2}\right)^5 + \frac{1}{7.3!}\left(\frac{\Delta\tau}{2}\right)^7 + \frac{1}{9.5!}\left(\frac{\Delta\tau}{2}\right)^9 + \cdots\right]. \tag{38}$$

ii) *Interpolation Procedure*

To evaluate equation (36), we require the values of both S and its first derivative with respect to τ; these quantities are to be supplied by the interpolation procedure. To compute the derivative we use the formula

$$\frac{dS}{d\tau} = -\frac{1}{\chi}\left(\mu\frac{\partial S}{\partial z} + \gamma\frac{\partial S}{\partial x}\right). \tag{39}$$

Hence our interpolation problem reduces to that of an accurate determination of χ, S, $(\partial S/\partial x)$, and $(\partial S/\partial z)$ at the point where a ray crosses a mesh line.

As we are always interpolating along mesh lines, the problem reduces to *one-dimensional* interpolation in x or in z. As was noted above, S and χ depend exponentially on x and z; therefore all interpolations are done for $\ln\chi$ and $\ln S$, which permits accurate determination of the needed quantities. The spatial derivatives are recovered from the formulae $(\partial S/\partial x) = S(\partial \ln S/\partial x)$ and $(\partial S/\partial z) = S(\partial \ln S/\partial z)$.

The opacity χ is determined by assuming that $\ln\chi$ is piecewise linear in z along lines of constant x and piecewise linear in x along lines of constant z. The optical-depth increment $\Delta\tau$ needed for the integration formula is found by assuming that $\ln\chi$ is piecewise linear in Δs; then $\Delta\tau = \Delta s(\chi_1 - \chi_0)/(\ln\chi_1 - \ln\chi_0)$, where χ_0 and χ_1 are determined by interpolation along the appropriate axis.

The corresponding problem for S is solved by a combination of cubic spline and parabolic interpolation. The spline continuity equation (Ahlberg, Nilson, and Walsh 1967) is used to pose separate systems for $\partial(\ln S)/\partial x$ and $\partial(\ln S)/\partial z$ along mesh lines of constant z and constant x, respectively. Boundary conditions for the spline system are supplied either by taking numerical derivatives of S at the endpoints of the mesh lines in nonperiodic cases, or by using the periodic spline boundary conditions for periodic media. Given the first derivatives obtained

from the solution of these tridiagonal systems, the piecewise cubic interpolating splines along the mesh lines are completely specified. Then, using the cubic splines, we can, for example, interpolate along the line $x = x_i$ to determine $\ln S(x_i, z)$ and $\partial[\ln S(x_i, z)]/\partial z$ for any value of z on a range $z_j > z > z_{j+1}$. We cannot, however, find $\partial[\ln S(x_i, z)]/\partial x$ in a similar manner unless we are willing to make spline estimates of $\partial^2(\ln S)/\partial x \partial z$, in which case we would have a true bicubic spline interpolant (which is costly to compute). Numerical experiments have shown that this is unnecessary. Satisfactory accuracy is obtained by parabolic interpolation in z of the values of $\partial[\ln S(x, z_j)]/\partial x$ generated at the points (x_i, z_j) by spline fits along the mesh lines $z = z_j$. With much lower cost in time and storage, the order of the result is the same as that obtained by using the full bicubic spline.

III. ILLUSTRATIVE EXAMPLES

In order to test the computational methods presented in § II and to gain some insight into two-dimensional transfer effects, we have computed a number of illustrative examples for semi-infinite atmospheres with periodic structures, and for freestanding slabs, both for static media and with velocity fields with amplitudes up to two fiducial Doppler widths. For all cases, in addition to the full two-dimensional (2D) solution, we have computed corresponding *multicomponent* and *spatially averaged* source term solutions. In the multicomponent models the *source function* is obtained by solving a one-dimensional (1D) transfer problem in, say z, at each value of x, *ignoring* lateral transport. By applying the full 2D *formal solution* to the multicomponent (1D) source function we obtain what we shall refer to as $1\frac{1}{2}$D radiation fields. By the "spatially averaged" solution we mean that straight averages of all physical quantities (ϵ, β, χ_c, etc.) were taken in the x-direction and then a single 1D transfer problem was solved in the z-direction using these mean quantities. The velocity field was averaged in the microturbulent limit; i.e., we set $\langle\Delta\rangle^{-1} = [\langle\Delta(x, z)^{-2} + v_z^2\rangle]^{1/2}$.

a) Periodic Media

The basic questions to be answered by a full two-dimensional radiative transfer solution are: (1) How do lateral transport effects change the emergent and internal radiation fields? (2) How valid is the computationally simpler $1\frac{1}{2}$D solution? (3) Can we infer the mean radiation field from a mean atmospheric model? Finally, (4) How are velocity diagnostics affected? A complete answer to these questions would require investigation of an enormous variety of cases. In this paper we make a start by presenting results for an exponential atmosphere with periodic horizontal disturbances. Although the models are idealized, the parameters have been chosen to be consistent with typical solar values. In most cases we have taken $X = 1000$ km which is near the limit of resolution; zero incident radiation; $B(x, z) = 1 + 1.5\tau_c$, where τ_c is the vertical continuum optical depth; and $\chi_c = 10^{-7} \exp(-0.01z)$. A few cases were computed with $X = 100$ km, which is below the limit of resolution, and is comparable to the vertical scale height.

On the basis of scaling-rule arguments (e.g., Jones and Skumanich 1977) one would expect that for $X = 1000$ km, two-dimensional transfer effects should be neglible, essentially because the photon diffusion path-length is effectively truncated by the swift variation of material properties in the z-direction; for $X = 100$ km, two-dimensional effects would be expected to occur. In actual fact, *we have not found a single instance of a significant difference between the* $1\frac{1}{2}$D *and* 2D *solutions for any of the periodic cases that we have considered.* It is still conceivable, however, that if fluctuations with nonzero averages, or embedded structures with enormous variations of material properties at a contact discontinuity, were considered, significant two-dimensional effects might be found. But in view of the results obtained here, we are somewhat skeptical that *major* two-dimensional effects are to be found in most situations of practical interest.

i) *Case I*

The simplest variation to study is a periodic change in the line strength. We have considered cases with $\epsilon(x, z) \equiv \epsilon_0$, and $\beta(x, z) = \beta_0[1 - 0.5 \cos(2\pi x/X)]$, with $\epsilon_0 = 10^{-3}$ or 1, and $\beta_0 = 3$, 10, 30, or 100.

The conclusions in all cases are similar. As expected, the line is shallower at $x = 0$ than at $X/2$, as illustrated in Figure 3*a*. There are substantial differences between the 1D and 2D line source functions near the surface (see Fig. 3*b*), which are always in the sense that 2D transfer effects reduce the lateral variations of the source function. But there is essentially no difference in the emergent intensities given by the $1\frac{1}{2}$D (multicomponent) and the full 2D solutions (see Fig. 3*c*). The maximum difference found, for $\beta_0 = 100$, was 8%; for $\beta_0 = 3$ the difference decreased to only 1%. As a consequence, the $1\frac{1}{2}$D solution gives almost identical variations of equivalent width $W(x)$ with position (see Fig. 3*d*). The spatial average of W is identical for the $1\frac{1}{2}$D and 2D solutions, and is well approximated by that computed from the spatially averaged source-term model. We find no evidence for significant two-dimensional transfer effects upon observable parameters in this case.

ii) *Case II*

A greater range of variation in the solution can be obtained by varying both ϵ and β. We adopted $\epsilon(x, z) = \epsilon_0[1 - 0.5e^{0.001z} \cos(2\pi x/X)]$ and $\beta(x, z) = \beta_0[1 + 0.5e^{0.001z} \cos(2\pi x/X)]$, which give a caricature of possible effects of pressure fluctuations from a wave propagating in an exponential atmosphere. We considered cases with

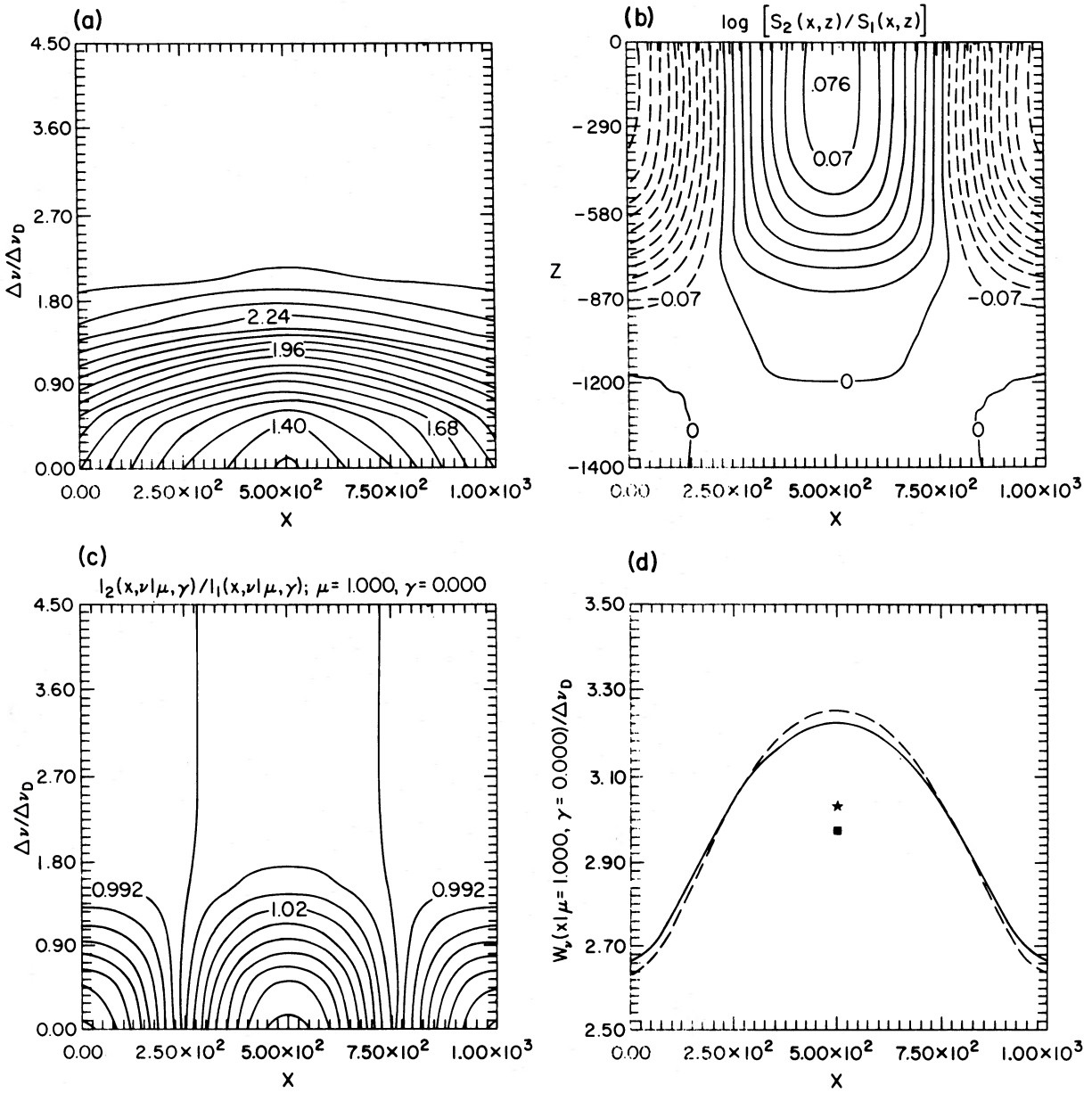

FIG. 3.—Source functions and observables for case I, defined in the text, with $\epsilon_0 = 10^{-3}$ and $\beta_0 = 10^2$. Both x and z are in km. (*a*) Contour diagram of $I_2(x, \nu)$, the 2D emergent intensity along the normal to the atmosphere, as a function of x and $\Delta\nu/\Delta\nu_D$*. In this and all subsequent figures, the subscript 1 denotes the 1½D solution and 2 denotes the 2D solution. (*b*) Contour diagram of $\log [S_2(x, z)/S_1(x, z)]$ as a function of x and z. Solid contours denote positive values; dashed contours denote negative values. (*c*) Contour diagram of $I_2(x, \nu)/I_1(x, \nu)$ as a function of x and $(\Delta\nu/\Delta\nu_D^*)$ for radiation emergent normally from the atmosphere. (*d*) Variation of equivalent width (in Doppler units) as a function of position. *Dashed curve*, 1½D solution; *solid curve*, 2D solution; *square*, horizontal average of 1½D and 2D results; *star*, equivalent width from horizontally averaged source terms.

$\epsilon_0 = 10^{-3}$ and 10^{-1}, and $\beta_0 = 1$, 10, 10^2, and 10^4. Because β is largest and ϵ is smallest at the edges of the cell, the surface value of the source function will be smallest there, and the line strength the largest.

As seen in Figure 4*a*, both the 1D and 2D source functions have significant spatial fluctuations at the surface. The full spatial variation of the 2D source function is shown in Figure 4*b* and the ratio S_2/S_1 in Figure 4*c*. Again the 2D solution shows only a weak lateral variation. The emergent intensity from the 2D solution is shown in Figure 4*d*. The line profile has a pronounced x-variation which yields the rather unusual spatial average shown in Figure 4*e*. The spatial variation of the equivalent width is shown in Figure 4*f*; the results from the 1½D and 2D solutions are essentially identical, and further, the spatial average of W is the same for both solutions and is

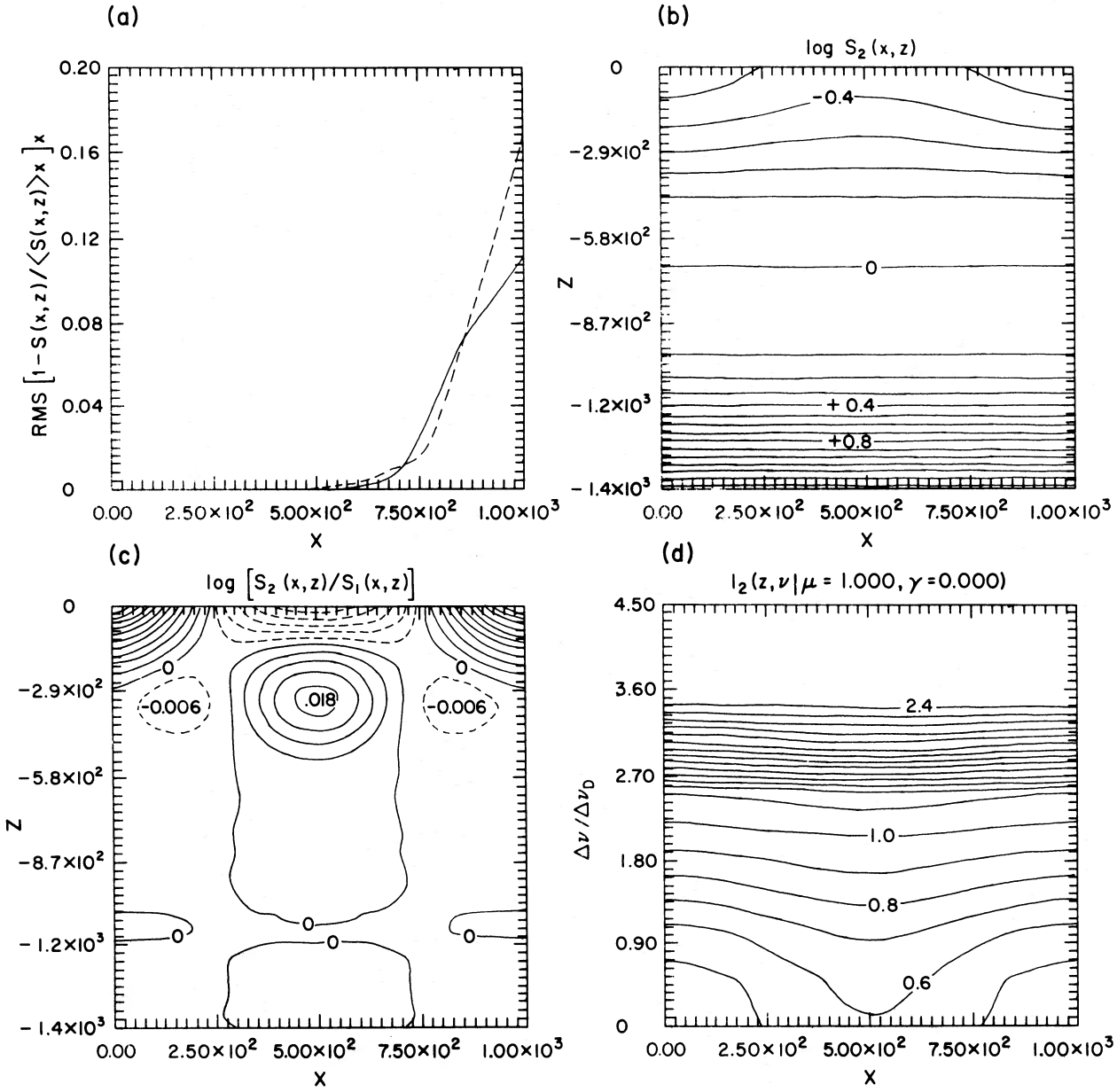

FIG. 4a–d

FIG. 4.—Source functions and observables for case II, defined in the text, with $\epsilon_0 = 10^{-1}$ and $\beta_0 = 10^4$. Coding of curves and plots are as in Fig. 3. (*a*) RMS fluctuation of source function relative to its horizontal average, as a function of z. *Dashed curve*, 1D solution; *solid curve*, 2D solution. (*b*) Contour diagram of $\log S_2(x, z)$ as a function of x and z. (*c*) Contour diagram of $\log [S_2(x, z)/S_1(x, z)]$, for *antiphase* variation of ϵ and β, as a function of x and z. (*d*) Contour diagram of $I_2(x, \nu)$, the emergent intensity from the 2D solution, as a function of x and $\Delta\nu/\Delta\nu_D$* for radiation emergent normally from the atmosphere. (*e*) Horizontal average of the line profile. The 1½D, 2D, and horizontal averaged source-term results are indistinguishable. Ignore physical units stated in ordinate table, as arbitrary units were employed. (*f*) Variation of equivalent width (in Doppler units) as a function of position for *antiphase* variation of ϵ and β. (*g*) Contour diagram of $\log [S_2(x, z)/S_1(x, z)]$, for *in-phase* variation of ϵ and β, as a function of x and z. Compare with Fig. 4*c*. (*h*) Variation of equivalent width as a function of position for *in-phase* variation of ϵ and β. Compare with Fig. 4*f*.

almost indistinguishable from that given by the spatially averaged model. The differences are even smaller for $X = 100$ km. We find no important effects of two-dimensional transport upon the line profiles or equivalent widths in any of these cases.

An interesting comparison is obtained by choosing the same $\epsilon(x, z)$ but now setting

$$\beta(x, z) = \beta_0[1 - 0.5e^{0.001z} \cos(2\pi x/X)];$$

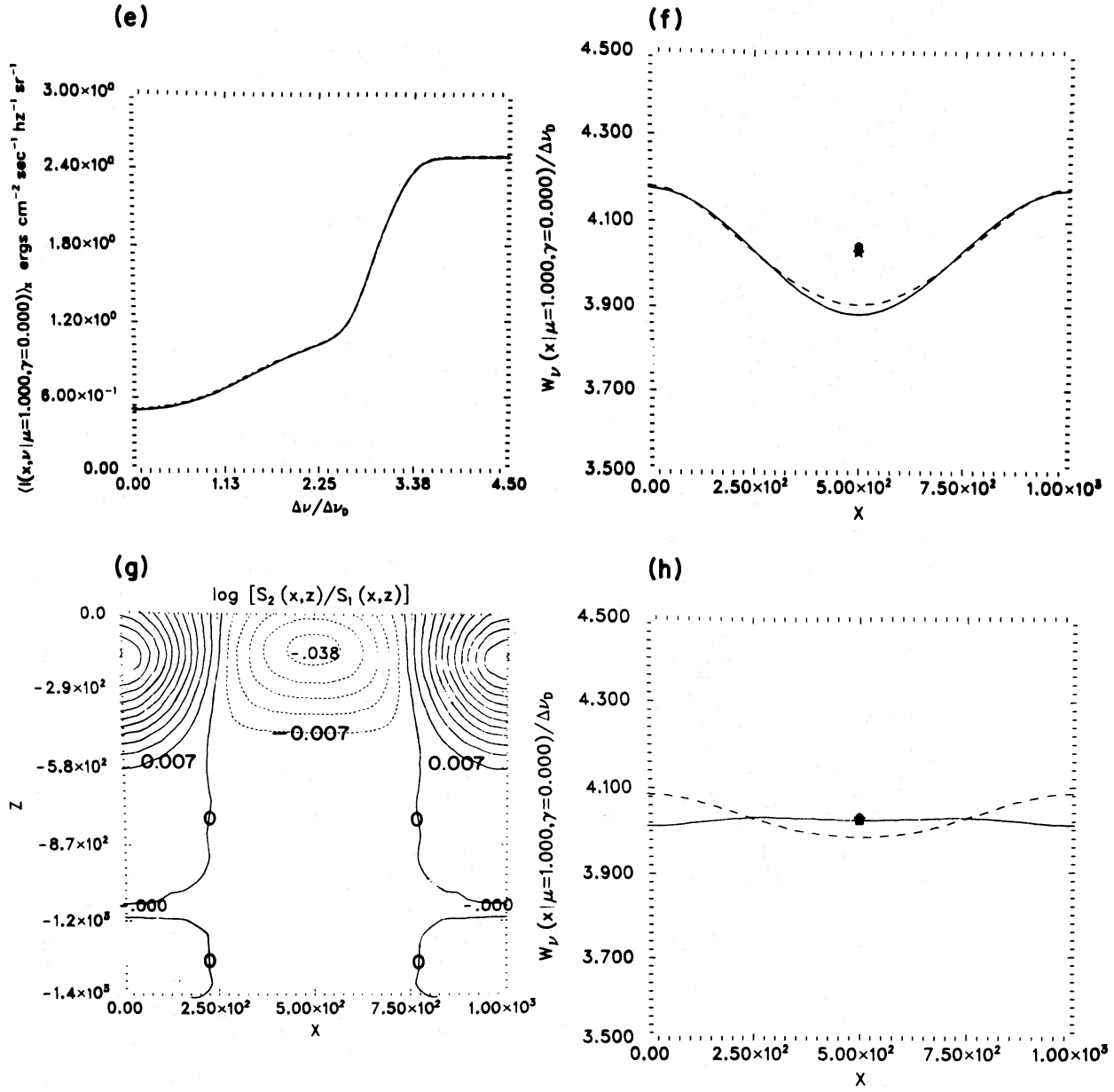

FIG. 4e–h

here the fluctuations in ϵ and β are mathematically in phase but physically tend to work against one another. The ϵ-variation predominates, and S is lower and W is greater at all boundaries than at cell center. As seen in Figure 4*h*, the variation of W for the multicomponent model is qualitatively the same as in Figure 4*f*, but with much smaller amplitude. In contrast, the 2D solution yields practically no variation (it even shows a weak antiphase variation). This occurs because ϵ is smallest where the line strength is smallest; hence the photon diffusion length is markedly increased, and the rise of S_2 relative to S_1 is now large enough to almost obliterate the horizontal variation of S_2 (see Fig. 4*g*).

iii) *Case III*

In the analysis of the solar spectrum, one frequently encounters line profiles that have been modified by velocity fields. The questions of how to solve the transfer equation, and of the relation of observed line-shift and line-asymmetry parameters, must then be faced. As a simple example we have considered a periodic medium with

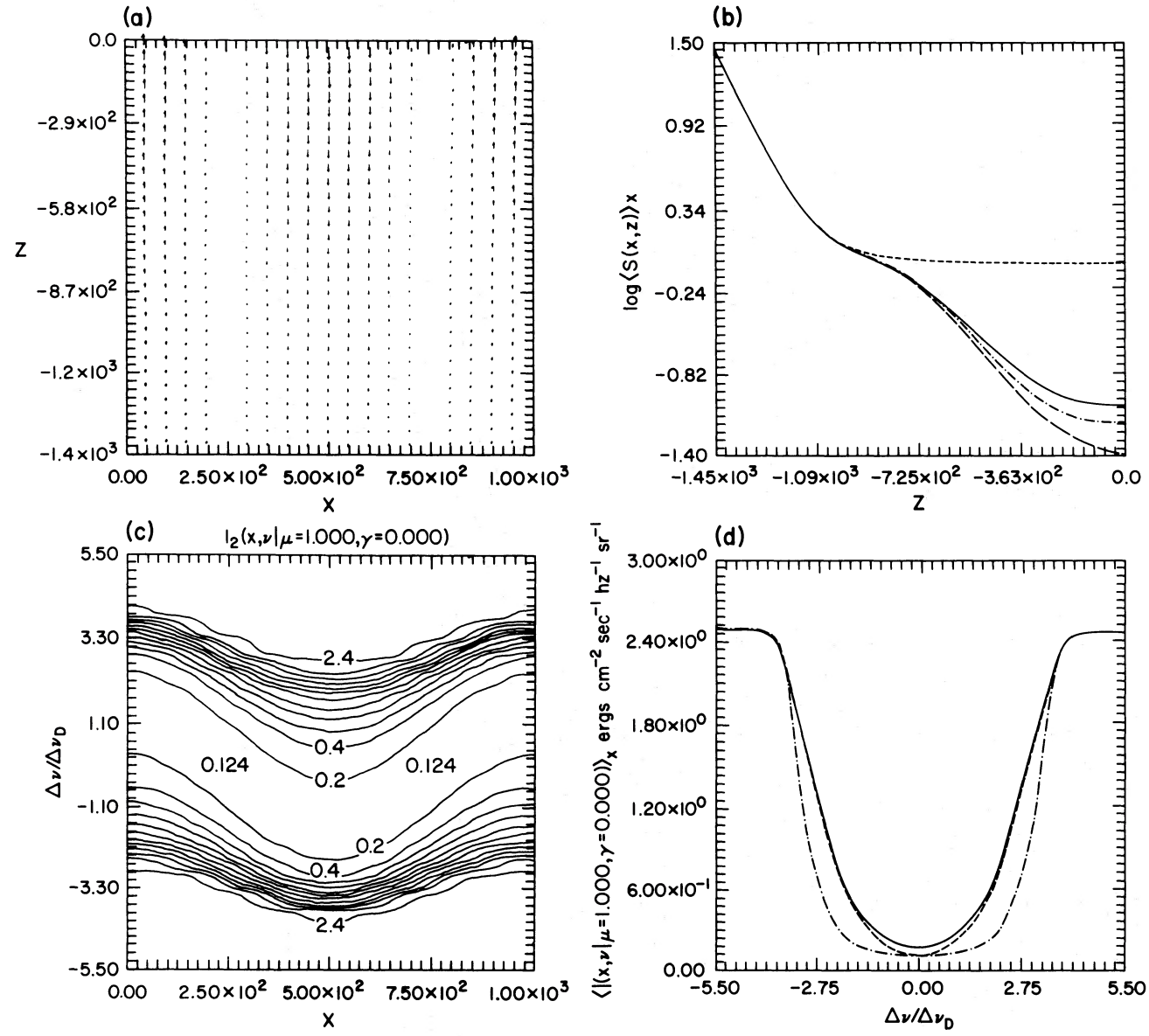

FIG. 5a–d

FIG. 5.—Properties and computed results for case III, defined in text, with $\beta_0 = 10^4$ and $V_{z0} = 2$. (*a*) Velocity field as a function of x and z; arrows give vector velocities. (*b*) Horizontal averages of source functions. *Short dashes*, Planck function. *Solid curve*, 2D solution. *Long dashes*, 1D (multicomponent) solution. *Dot-dash curve*, horizontally averaged source-terms. (*c*) Contour diagram of $I_2(x, \nu)$, emergent intensity from 2D solution. Line of sight is normal to atmosphere. (*d*) Horizontal average of line profiles. *Solid curve*, 2D solution; *dashed curve*, $1\frac{1}{2}$D solution; *dot-dashed curve*, horizontally averaged source-terms with velocities treated in microturbulence limit. Note overestimate of velocity-field effects in latter case. (*e*) x-position of point at unit optical depth along ray with direction cosines (μ, γ) penetrating out of atmosphere at horizontal positions x_0, as a function of x_0 and $\Delta\nu/\Delta\nu_D$*. (*f*) Same as (5*e*) for z-position of point at unit optical depth on ray.

geometric properties and values of χ_c and B as specified above, for lines with $\epsilon \equiv 10^{-3}$, $\beta \equiv \beta_0$, and a velocity field of the form $v_z(x, z) = v_{z0} \exp(0.001z) \cos(2\pi x/X)$ which is shown in Figure 5*a*. The velocity has a sinusoidal x-variation whose amplitude decays with increasing depth into the atmosphere. We treated cases with $\beta_0 = 10^4$, 10^2, and 10, and $v_{z0} = 1$ and 2; these are labeled III*a*–III*f* as specified in Table 1. An extensive series of runs was made with different numbers of angle-points in order to determine how the solution is affected by the quadrature. In all cases we found that six points per octant gave essentially identical results to the choice of 12 per octant. The Eddington approximation (one point per octant) was accurate to about $\pm 10\%$ in S for $v_{z0} = 0$ or 1, but

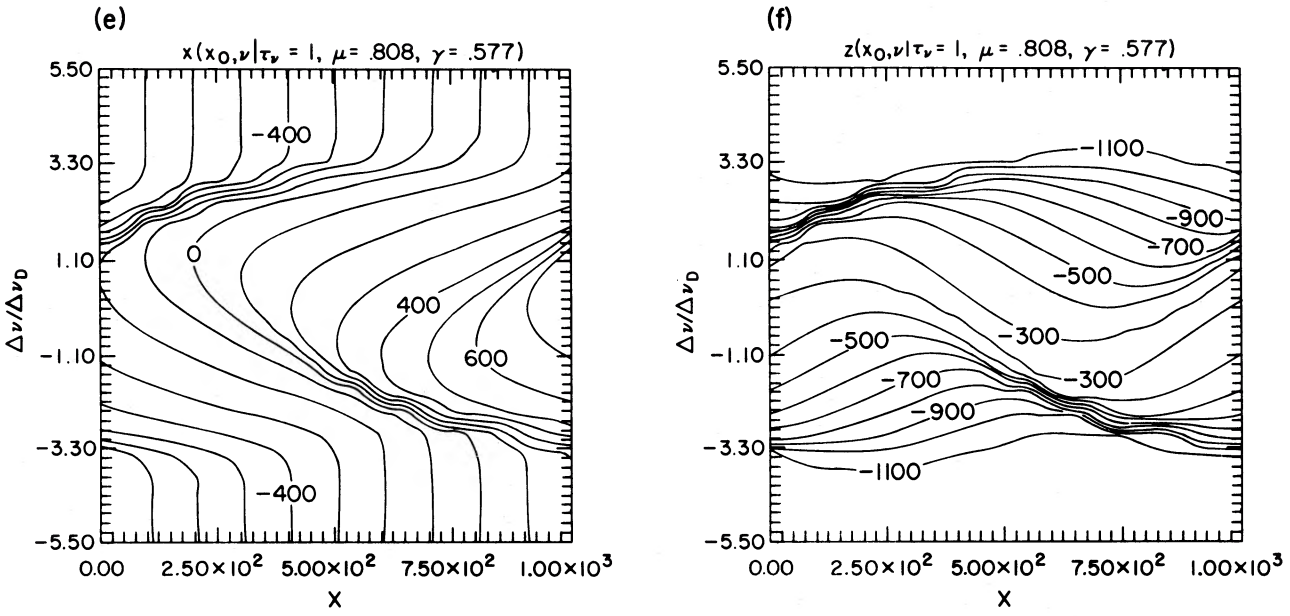

FIG. 5e–f

deteriorated to errors of $\pm 20\%$ in S for $v_{z0} = 2$. All the results displayed in the figures are based on a six-point quadrature.

As was mentioned in § II, the Hermitian ray-integration technique showed decisive superiority over difference equations moving media. In particular, the solutions showed a precise symmetry around the point $(x/X) = \pi/2$, which is implicit in the form of $v_z(x, z)$, but which is *not* explicitly *imposed* in the computation. In contrast, the difference-equation solution failed to have symmetry around this point and exhibited unacceptably large oscillations in S at successive x-points in the grid. Our experience suggests that of the two methods only the Hermitian method can be used when velocity fields are present.

As is true for cases I and II described above, observable quantities from the $1\frac{1}{2}$D and 2D solutions are practically identical. As before, S_2 can differ substantially from S_1, always in the sense of being much more constant as a function of x, but the detailed x-variation of the emergent intensities, equivalent widths, line shifts, and line widths from the two solutions are indistinguishable; hence the multicomponent ($1\frac{1}{2}$D) treatment suffices in this case. The depth variation of the horizontal average $\langle S(x, z)\rangle_x$ for the 1D, 2D, and spatially averaged solutions in case III*b* are shown in Figure 5*b*. The maximum values of I_2/I_1 for the emergent intensities are 1.12, 1.68, 1.03, 1.11, 1.01, and 1.02 for cases III*a*–III*f*, respectively; these all occur at line center, and except for case III*b* are negligible. The equivalent widths computed from the $1\frac{1}{2}$D and 2D solutions agree to within 2% for case III*b* and to within 1% or less for the other case.

As can be seen in Figure 5*c*, the emergent line profiles faithfully indicate the vertical velocity field. Horizontal averages of the $1\frac{1}{2}$D and 2D profiles are virtually identical (see Fig. 5*d*), but the effect of the velocity field on the line width is grossly overestimated in the spatially averaged solution. This shows that a treatment of velocity fields in the microturbulence limit exaggerates their effects; conversely, if one *deduces* velocity field from calculations using the microturbulence limit, one tends to underestimate their amplitude.

TABLE 1

LINE-SHAPE AND LINE-STRENGTH PARAMETERS FOR CASE III*

Case	β_0 (1)	V_{z0} (2)	$\Delta\nu_0$ (3)	z_0 (4)	$V_z(z_0)$ (5)	$\Delta\nu_{1/2}$ (6)	$\delta_{1/2}$ (7)	$z_{1/2}$ (8)	$V_z(z_{1/2})$ (9)
III*a*.....	10^4	1	0.78	−290	0.75	0.42	5.40	−1000	0.37
III*b*.....	10^4	2	1.54	−290	1.50	0.83	5.53	−1000	0.74
III*c*.....	10^2	1	0.51	−745	0.48	0.38	3.75	−1040	0.35
III*d*.....	10^2	2	1.01	−745	0.96	0.77	3.78	−1040	0.70
III*e*.....	10	1	0.41	−960	0.38	0.36	2.75	−1040	0.35
III*f*.....	10	2	0.82	−960	0.76	0.73	2.77	−1040	0.70

* Detailed properties of this case are specified in text. Frequency displacements and velocities are in units of the fiducial Doppler width $\Delta\nu_D$*. Depths are in km. Viewing angle is normal to atmosphere ($\mu = 1.0$, $\gamma = 0.0$).

Detailed information on line-strength and line-shape parameters is given in Table 1. Each case is characterized by a choice of β_0 and v_{z0}, listed in columns (1) and (2). Frequency positions of line center, $\Delta\nu_0$, and the half-intensity bisector, $\Delta\nu_{1/2}$, at spatial position $x = 0$ (maximum upward velocity) are given in columns (3) and (6), and the full half-intensity width $\delta_{1/2}$ is given in column (7). The physical depth z_0 at unit optical depth at line center is given in column (4), and $v_z(z_0)$ is given in column (5).

From the Eddington-Barbier relation we expect that the emergent intensity at line center is dominated by contributions from depth z_0; hence $\Delta\nu_0$ should very nearly equal $v_z(z_0)$. We see that $\Delta\nu_0$ does quite accurately reproduce $v_z(z_0)$, and that this equality is more closely realized for stronger lines; that $\Delta\nu_0$ is always greater than $v_z(z_0)$ follows from the fact that the intensity is not determined at *exactly* $\tau = 1$, but includes contributions from higher layers. A similar comparison can be made between the position of the half-intensity bisector $\Delta\nu_{1/2}$ and the velocity $v_z(z_{1/2})$, where $z_{1/2}$ (given in col. [8]) denotes the physical depth corresponding to unit optical depth at the frequency positions of the half-intensity points in the profile (i.e., at $\Delta\nu = \Delta\nu_{1/2} \pm \frac{1}{2}|\delta_{1/2}|$). Comparison of $\Delta\nu_{1/2}$ with $v_z(z_{1/2})$ shows that good agreement is obtained for relatively weak lines, but that $\Delta\nu_{1/2}$ becomes systematically larger than $v_z(z_{1/2})$ as the line strength increases. As pointed out by Kulander and Jefferies (1966), this results from a contribution of overlying layers, moving at larger velocities, to the line profile intensity; one expects a systematic deterioration of the accuracy with which the bisector position reproduces the actual velocity as one uses points progressively farther from line center.

The results described above all refer to a viewing angle normal to the surface of the atmosphere, i.e., $\mu = 1.0$, $\gamma = 0.0$. When one examines the structure obliquely, complicated projection effects can occur. To illustrate these, we show in Figures 5*e* and 5*f* the spatial positions of the point at unit optical depth along a ray emerging at an angle with direction cosines (μ, γ) as a function of x_0, the x-position where the ray emerges from the medium, and $\Delta\nu/\Delta\nu_D$*, the frequency displacement from line center. The plots show that if we look at a given position on the disk then at different points in the profile we see to quite different physical positions (x, z) in the medium. These results emphasize the difficulty faced when one attempts to diagnose the velocity structure of the medium from observed line shifts, and demonstrate that simple techniques that associate a unique spatial point with the velocity field inferred from a profile are gross oversimplifications of reality, and may be untrustworthy. On the other hand, diagrams such as Figures 5*e* and 5*f*, when computed for specific solar-atmospheric structures, with realistic model parameters, offer the possibility of much-improved accuracy in the diagnostic technique.

iv) *Case IV*

An opportunity for significant two-dimensional transfer effects arises when there are both vertical and horizontal velocity components. In the one-dimensional solution for the *source functions*, v_x is *ignored* (the direction cosine γ having been suppressed); but given the 1D source function, *both* v_x and v_z are taken into account in the $1\frac{1}{2}$D *formal solution*. We have chosen a velocity field $v_x = v_{x0} \exp(0.001z) \sin(2\pi x/X)$ and

$$v_z = v_{z0} \exp(0.001z) \cos(2\pi x/X),$$

which, as shown in Figure 6*a*, provides a caricature of an upwelling periodic medium. We again used the case I–III values of χ_c and B and set $\epsilon \equiv 10^{-3}$, $\beta \equiv \beta_0$. We considered the values $\beta_0 = 10^4$, 10^2, and 10, and $v_{x0} \equiv v_{z0} = -1$ or -2. All results reported here were obtained using six angle points per octant.

The source function ratio S_2/S_1 shows an interesting dependence upon β_0. For $\beta_0 \leq 10^2$, the line thermalizes in the continuum, rather than being thermalized by collisions ($\epsilon = 10^{-3}$). Thus the effect of accounting for *both* velocity components in the 2D solution is to *increase the escape probability* relative to the 1D solution. Thus S_2 drops below S_1, and for cases with $(\beta_0, |v_{x0}|) = (10, 1)$, $(10, 2)$, $(100, 1)$, and $(100, 2)$, the minimum values for S_2/S_1 are 0.83, 0.79, 0.94, and 0.87, respectively. In these cases the 2D equivalent widths are greater than the 1D equivalent widths, by about 3% for $\beta_0 = 10$ and about 1% for $\beta_0 = 100$. When $\beta_0 = 10^4$, the line thermalized by collisions above the point of continuum formation. In this case $S_2/S_1 > 1$ because now the line shifts allow incident continuum photons from below to be intercepted. In these cases $W_2 < W_1$, with about a 5% difference for $(\beta_0, |v_{x0}|) = (10^4, 2)$.

As was true in case III, the x-dependence of line-shift parameters $\Delta\nu_0$ and $\Delta\nu_{1/2}$ and of the line-width parameter $\delta_{1/2}$ are virtually identical for the 2D and $1\frac{1}{2}$D solutions. Also, the spatial averages of the line profiles are nearly identical for both solutions, and again the microturbulence treatment of the velocity field in the spatially averaged solution yields much too broad a line profile.

If viewed at normal incidence, the line profiles in this case are virtually the same as in case III. Viewed obliquely, one sees effects of both v_z and v_x. Again the line center displacement $\Delta\nu_0$ provides an accurate estimate of the line-of-sight projection of the velocity, $v = \mu v_z + \gamma v_x$. A typical example is shown in Figure 6*b*; by tracing the rays downward at the angles indicated to $z_0 = -270$ in Figure 6*a*, one can readily verify the correctness of the line-shifts shown in Figure 6*b*. As was true in case III, the (x, z) positions of unit optical depth along the ray, shown in Figures 6*c* and 6*d*, are quite complicated functions of x_0, the position of observation, and $\Delta\nu/\Delta\nu_D$* in the profile; again a difficult diagnostic problem is faced when one attempts to infer the spatial variation of the velocity field.

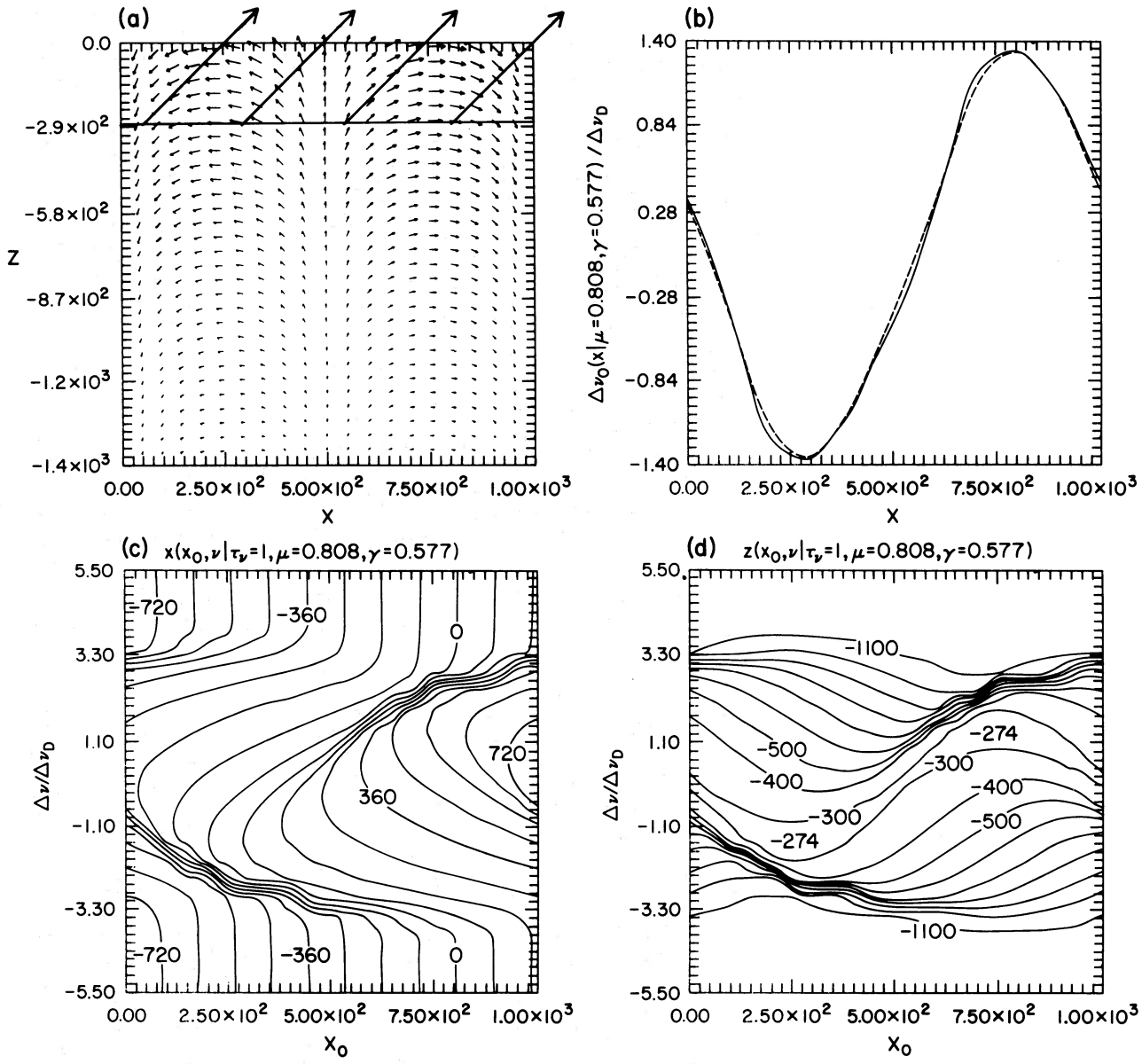

FIG. 6a–d

FIG. 6.—Properties and computed results for case IV defined in text, with $\beta_0 = 10^4$ and $|V_{x0}| = |v_{z0}| = 2$. (*a*) Velocity field; arrows give vector velocities. Rays with direction cosines $(\mu, \gamma) = (0.808, 0.577)$ are sketched emerging from the medium at $x = 250$, 500, 750 and 1000 km. The horizontal line at $z = -270$ km is the locus of line center unit optical depth along these rays. (*b*) Line-center displacement $\Delta\nu_0$ (in fiducial Doppler widths) seen at a viewing angle with $(\mu, \gamma) = (0.808, 0.577)$ so that both vertical and horizontal velocity components contribute. Comparison with Fig. 5*a* shows that the shifts are precisely what would be expected from the velocity field at unit optical depth along the rays. Note that $1\frac{1}{2}$D results (*dashes*) and full 2D results are nearly identical. (*c*) Same as Fig. 5*e* for case IV. (*d*) Same as Fig. 5*f* for case IV.

Again we conclude that the multicomponent ($1\frac{1}{2}$D) treatment of the problem is sufficient, though this may not be true for all possible choices of model parameters.

b) Freestanding Slabs

The effects of two-dimensional transfer are expected *a priori* to be much larger for freestanding slabs, where photons may leak out of (or into) the sides of the material as well as the top. We have considered a series of cases for a constant-density slab with $X = 5000$ km, $Z = -30{,}000$ km, $\chi_c \equiv 4 \times 10^{-5}$ (so that the total x-direction continuum optical thickness is 0.2), $B \equiv 1$, $\beta \equiv 10^3$, and with various values of $\epsilon \equiv \epsilon_0$, of v_{x0} in a velocity law $v_x = v_{x0} \cos(\pi x/X)$, and of I_0, the intensity incident from below on both the bottom and sides of the slab. The

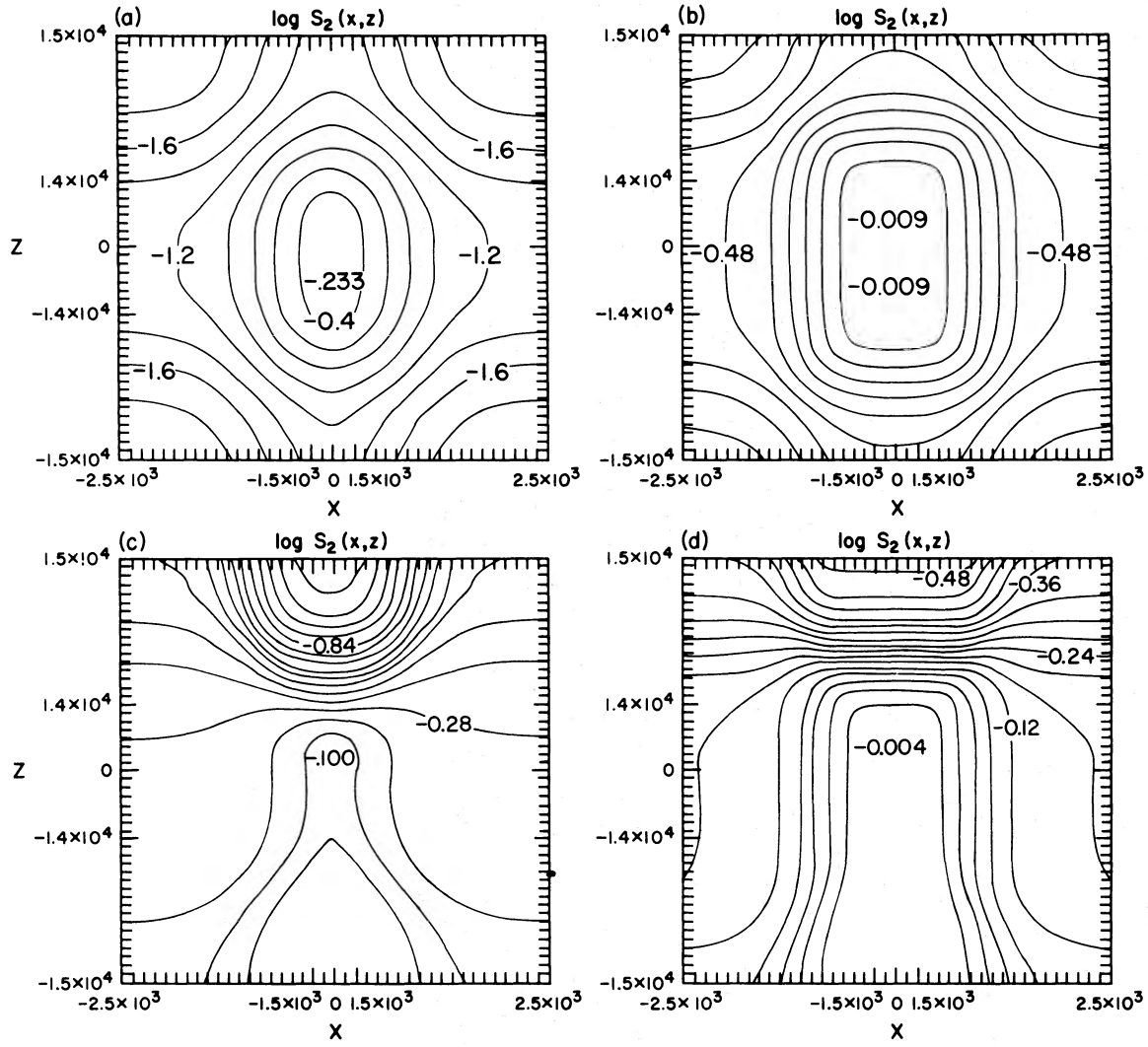

FIG. 7a–d

FIG. 7.—Contour diagrams of 2D source function for freestanding slabs. Ordinate and abscissa are logarithmically spaced; see text for discussion. Figs. 7*a*–7*f* refer to cases V*a*–V*f*, respectively, as defined in Table 2.

intensity from above, on both the top and sides, was set to zero. In both the x- and z-directions a logarithmic grid of the type shown in Figure 2 was employed in order to obtain an appropriate variation of optical-depth steps at the boundary surfaces. The graphs have been labeled in physical units, but are plotted on the logarithmic scale in order to show the edge effects clearly. The reader should note that in z the points at $\pm 1.4 \times 10^4$ km, and in x the points at $\pm 1.5 \times 10^3$ km, are 10^3 km from the surface, so the graphs *greatly* expand the zones near the boundaries and compress the size of the central region of the slab.

We considered series of models with $\epsilon_0 = 10^{-3}$ and 10^{-1} corresponding to effectively thin and effectively thick (static) structures, respectively. We chose $I_0 = 0$, 1, and 100, corresponding to situations where (*a*) all radiation results from internal excitation within the slab, (*b*) the slab is irradiated with a field comparable to the internal thermal source term, and (*c*) the slab is irradiated with a strong source from below (e.g., chromospheric Lα incident upon a prominence). For convenience in discussion, letter designations are assigned to the different cases treated, whose properties are specified in Table 2. Because of the large number of gridpoints in the (x, z) mesh, only a limited number of angle-points were considered in order to allow us to explore a large number of cases with reasonable computational economy. We found that the Eddington approximation (one angle-point per octant) gave results that agreed to within $\pm 10\%$ with those obtained using three angle-points per octant for $|v_{x0}| = 0$ or 1; for $|v_{x0}| = 2$ the errors were $\pm 20\%$. All results quoted here are based on Eddington-approximation solutions.

Results for *static* slabs are shown in Figures 7 and 8. In Figure 7, the two-dimensional source function is plotted. Figures 7*a* and 7*b* show results for cases V*a* and V*b*, respectively. Here one finds that the source function decreases

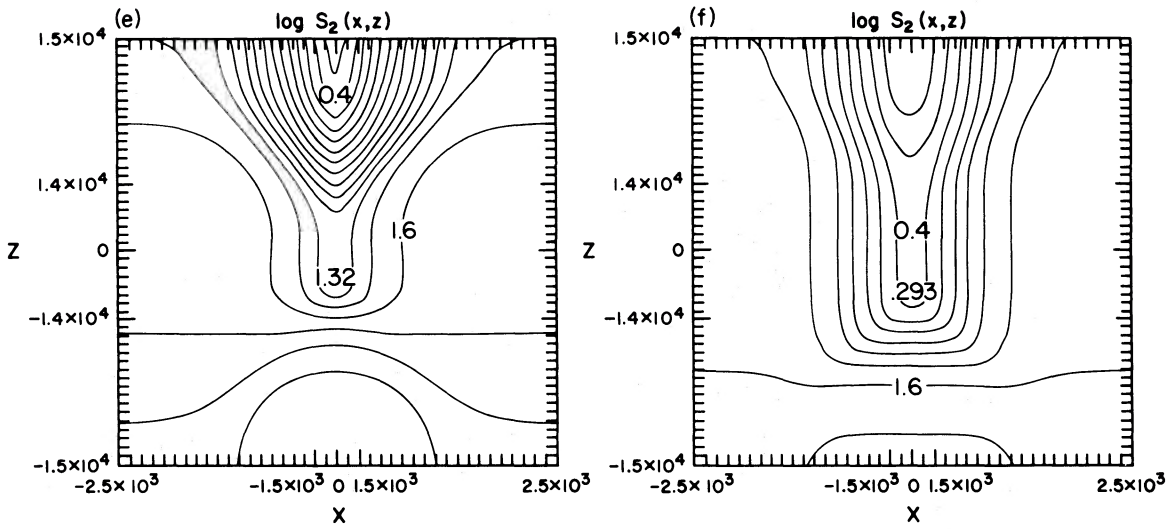

FIG. 7e–f

monotonically away from the slab center, and one sees large corner effects where the source function drops rapidly as a result of photon escapes in two directions. In case V*a*, which is effectively thin, S does not thermalize at slab center, whereas in case V*b*, which is effectively thick, it does. In Figures 7*c* and 7*d* we show log S for cases V*c* and V*d*, respectively, where the slab receives unit intensity from below. In both cases the minimum value of S is attained at the top of the slab on the axis of symmetry, and a relative minimum region extends downward into the slab; this results from the inner material being shielded from the incident radiation. Again in case V*c* the solution never thermalizes and the minimum at the top of the slab is much lower than it is for case V*d*, which does thermalize throughout a large fraction of the volume. Results for cases V*e* and V*f*, in which $I_0 = 100$, are shown in Figures 7*e* and 7*f*, respectively. Here the dominant effect on S is penetration by incident radiation; as the penetration occurs more efficiently when the destruction length for a photon is large, case V*e* with $\epsilon = 10^{-3}$ shows much *higher* internal excitation than case V*f* with $\epsilon = 10^{-1}$. The incident radiation penetrates about one thermalization depth in from the boundary.

Contour diagrams of the frequency and height dependence of the profiles are shown in Figure 8. These calculations were made for a geometric configuration appropriate to a structure seen at the limb; that is, the line of sight penetrates normally through the slab, and does not intercept the photosphere on the other side. The emission seen is thus the result of internal excitation and incident radiation (if any) scattered by the material into the line of sight. The bottom of the slab is on the left in these plots, and the top is on the right. In cases V*a* and V*b* (shown in Figs. 8*a* and 8*b*) the central core shows a profile identical to the 1D solution, and the intensity fades away at both the top and bottom of the slabs. At the center, one has a doubly reversed emission line, and at the upper and lower boundaries one finds an absorption feature. In cases V*c* and V*d* one has an extremely bright emission rim at the lower boundary. At the lower boundary and in the main body of the slab the profile is a doubly reversed emission feature. At the top boundary the line fades away and is a simple emission line. In cases

TABLE 2

PROPERTIES ASSIGNED TO FREESTANDING SLABS

Case	ϵ_0	V_{x0}	I_0
V*a*	10^{-3}	0	0
V*b*	10^{-1}	0	0
V*c*	10^{-3}	0	1
V*d*	10^{-1}	0	1
V*e*	10^{-3}	0	100
V*f*	10^{-1}	0	100
V*g*	10^{-1}	−1	0
V*h*	10^{-1}	−2	0
V*i*	10^{-1}	−1	1
V*k*	10^{-1}	−2	1
V*l*	10^{-1}	−1	100
V*m*	10^{-1}	−2	100

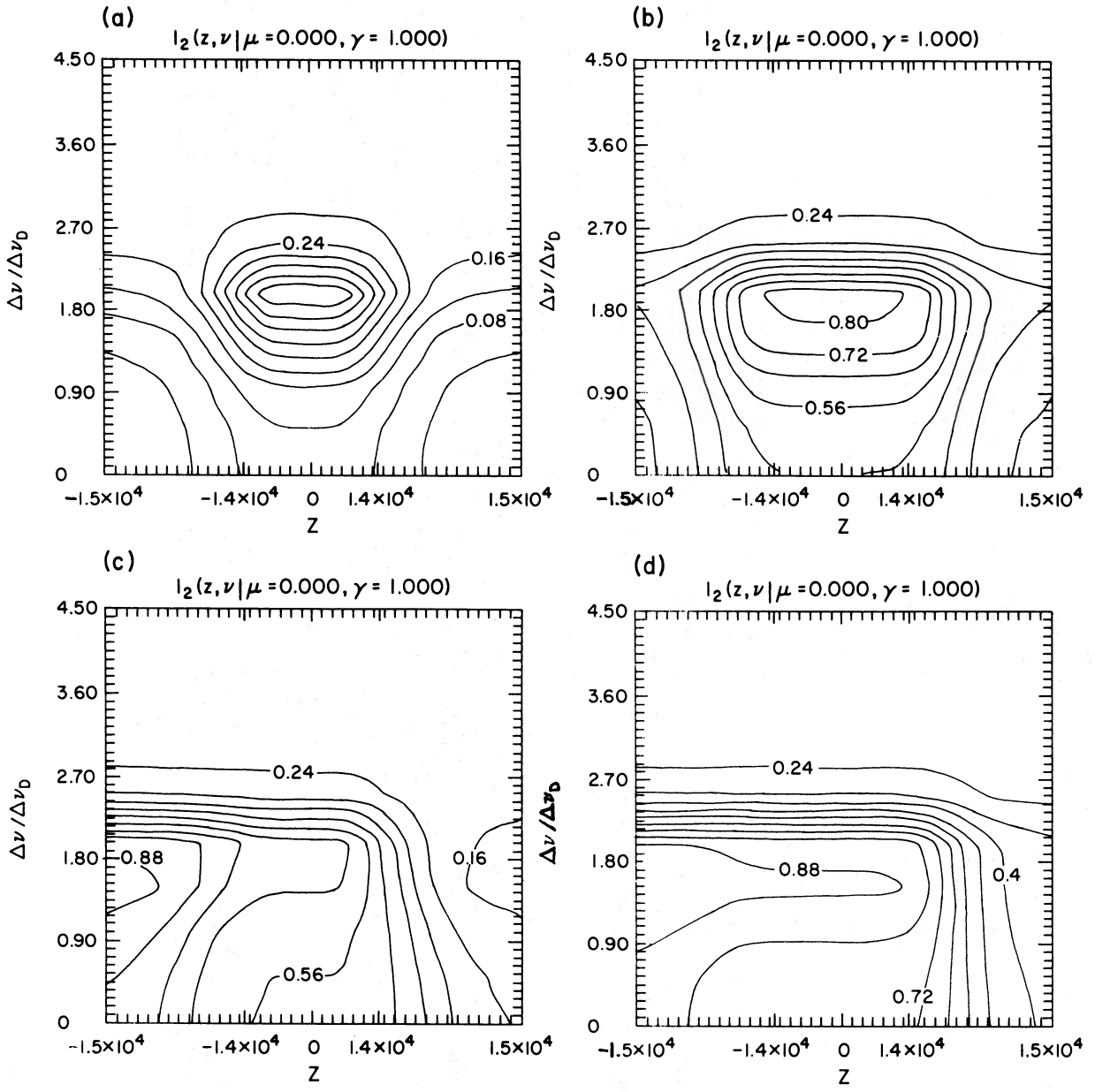

FIG. 8*a–d*

FIG. 8.—Contour diagram of $I_2(z, \nu)$, emergent intensity along line of sight normal to freestanding slab, using 2D source function. Figures 8*a*–8*f* refer to cases V*a*–V*f*, respectively.

V*e* and V*f* there is a bright emission rim at the lower boundary, and the profile is almost flat-topped. In the main body of the slab one sees a simple emission line that fades away toward the upper boundary.

For an expanding slab (with the velocity field illustrated in Fig. 9) we find that if $I_0 = 0$, the source function everywhere *decreases* throughout the slab because of the increased escape probability of photons; if $I_0 = 1$, the source function is essentially *unchanged* because losses from the increased probability of escape are approximately compensated by penetration of the incident field; if $I_0 = 100$, the source function *rises* because of increased penetration of the intense incident field. Contour diagrams of the spatial and frequency dependence of the profiles for cases V*g*–V*m*, whose properties are given in Table 2, are shown in Figure 10. Note that when $I_0 = 0$ we obtain th expected result of a blueshifted absorption component that partially suppresses the blueward emission peak. When $I_0 = 1$, a basically similar appearance is found, except that the absorption feature is weaker, and the profiles are almost flat-topped. For $I_0 = 100$, the radiation scattered into the line of sight from the external irradiation

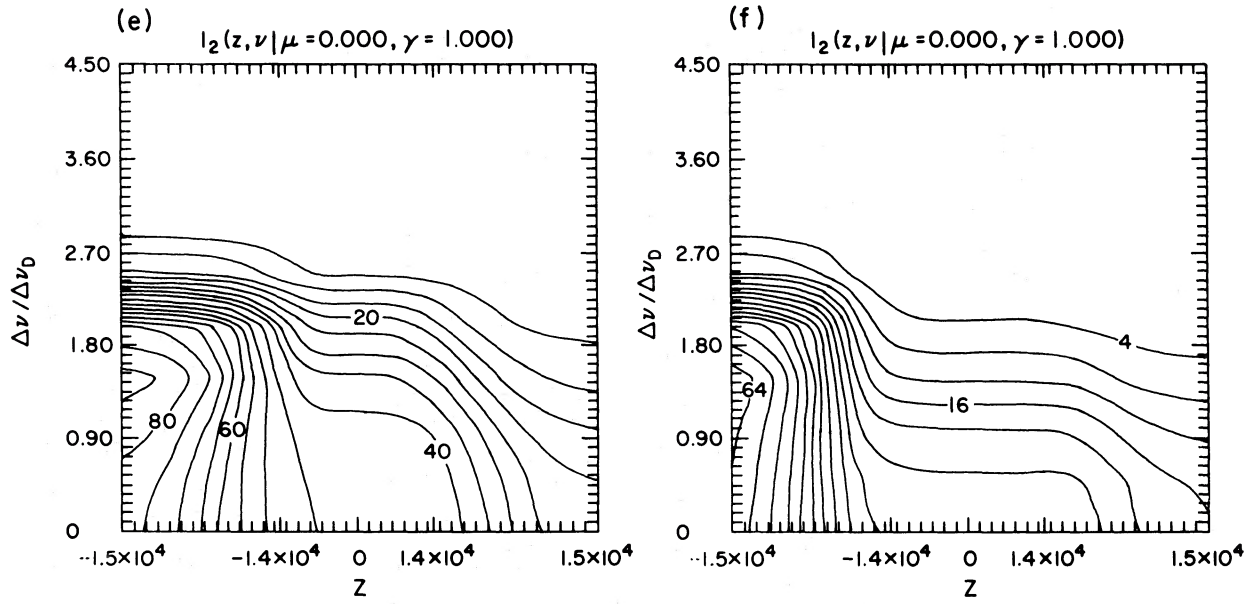

FIG. 8e–f

prevails over that generated internally, and one sees a blueshifted *emission* peak. The contrasting behavior in these cases shows that one must exercise care in attempting to infer velocity fields from observed profiles, for a naive interpretation of these profiles would lead to different velocity fields in each case, even though all of them result from a unique physical structure and velocity distribution.

IV. CONCLUSIONS

The solar literature abounds with statements about the potential importance of multidimensional radiative transfer. The method presented in this paper permits us, for the first time, to determine in a simple manner the validity of these statements in a routine way. The Hermite scheme is economical, flexible, and stable. In the form we have used it, it may be applied to essentially any two-level-atom problem in Cartesian coordinates, and generalization to cylindrical or other geometries is straightforward. The method guarantees the diffusion limit and is well conditioned in the presence of velocity fields. It should be applicable in other contexts, such as reactor calculations.

Our numerical tests show *absolutely no evidence for the importance of two-dimensional radiative transfer effects in exponential atmospheres.* In all cases we have found that a "multicomponent" model (i.e., the $1\frac{1}{2}$D solution)

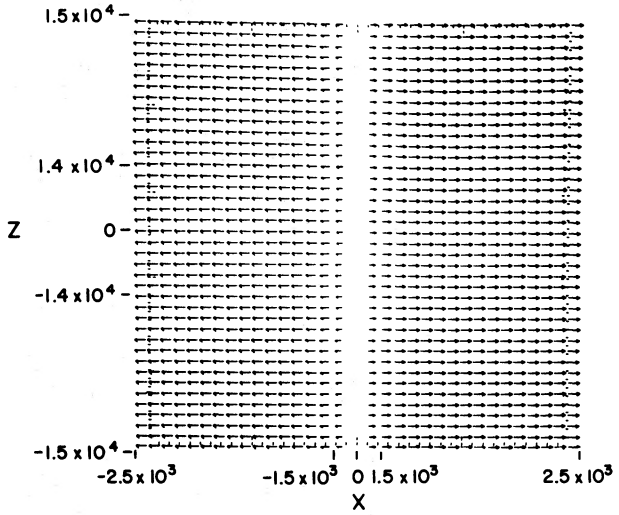

FIG. 9.—Velocity field for expanding freestanding slab

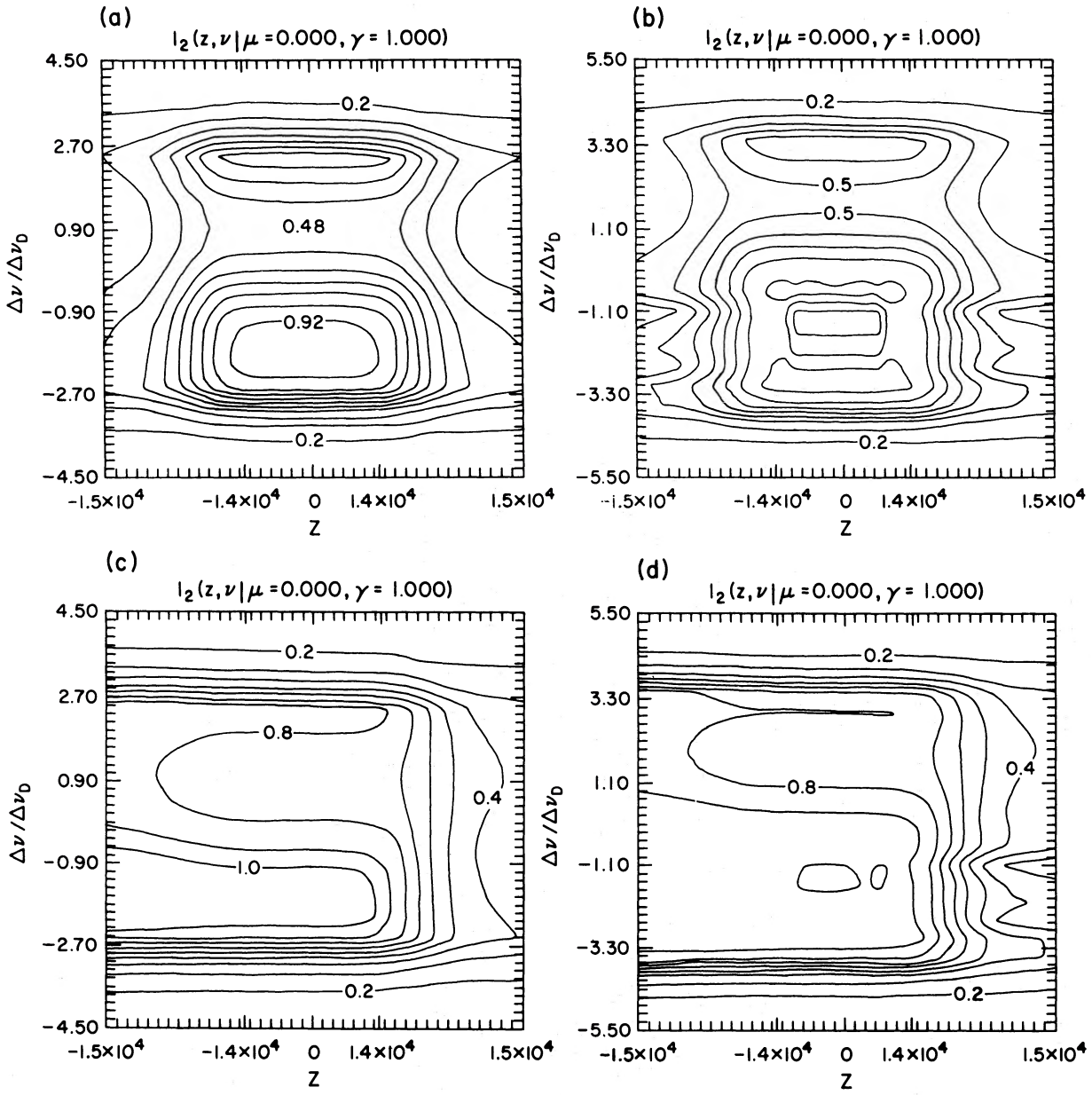

FIG. 10*a–d*

FIG. 10.—Contour diagrams of spatial and frequency dependence of intensity emergent normally from expanding freestanding slabs (cf. Fig. 8). Figs. 10*a*–10*f* refer to cases V*g*–V*m*, respectively. Note that in Figs. 10*e* and 10*f*, several of the contours were unfortunately mislabeled; all contours labeled with values less than unity should have the value given increased by a factor of 100.

adequately reproduces the emergent radiation field and, if anything, overestimates the response of the radiation field to fluctuations in the physical variables. While our investigation is, perforce, limited in scope, we feel it is unlikely that our conclusion is incorrect. Physically if the wavelength of the disturbance is greater than the scale height, lateral transport is unimportant and the multicomponent model is *a priori* valid; but if the wavelength is comparable or smaller than the scale height, then the lateral transport simply erases the effect of lateral inhomogeneities. In neither case can we get a significant effect. The possible importance of 2D effects can now be tested in any well-posed problem, and the burden of proof now lies upon any assertion of their relevance.

Two-dimensional transfer effects are likewise unimportant in the determination of macroscopic velocities in exponential atmospheres. The best diagnostic of this quantity appears to be the position of line center.

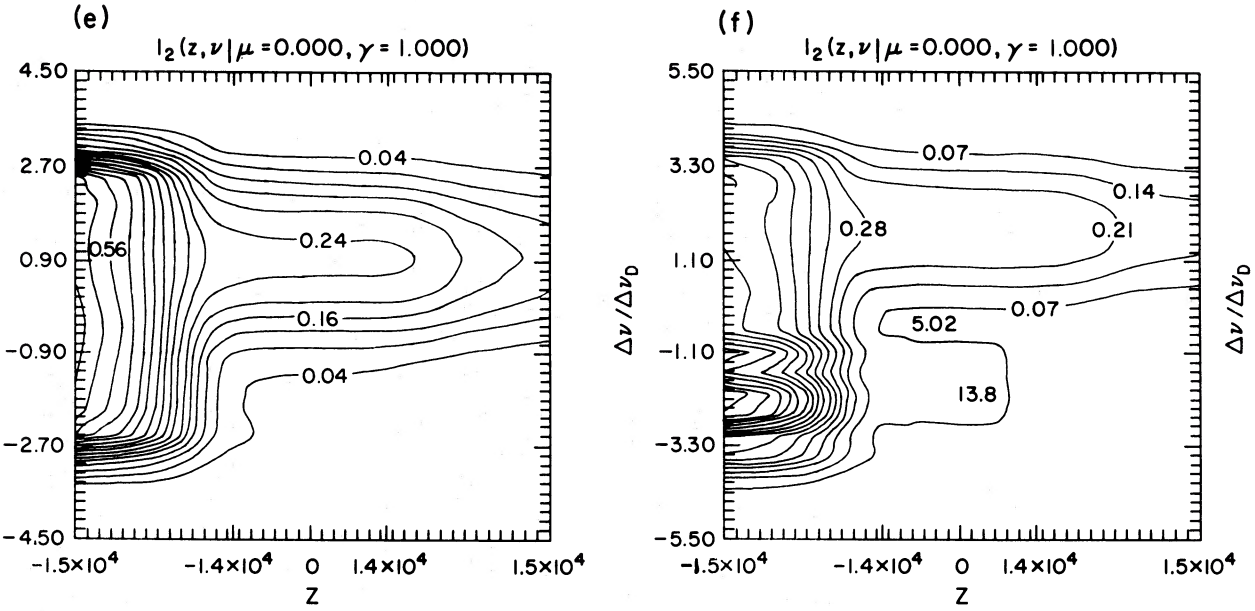

FIG. 10e–f

In our freestanding slab models we have found some evidence for two-dimensional effects at depths less than one thermalization length from the surface, but these boundary layers will be difficult to observe adequately. The emergent radiation field does show a large sensitivity to the strength of an externally imposed field.

Portions of the work on this project by one of us (B. R. M.) were supported in part by a Danforth Foundation Fellowship and by NASA grant NGL 06-003-057 to the University of Colorado.

APPENDIX A

DIFFERENCE EQUATION REPRESENTATION OF THE TWO-DIMENSIONAL TRANSFER EQUATION

In writing a difference equation representation of the differential equation

$$\frac{\mu^2}{\chi}\frac{\partial}{\partial z}\left(\frac{1}{\chi}\frac{\partial u}{\partial z}\right)+\frac{\mu\gamma}{\chi}\frac{\partial}{\partial z}\left(\frac{1}{\chi}\frac{\partial u}{\partial x}\right)+\frac{\partial}{\partial x}\left(\frac{1}{\chi}\frac{\partial u}{\partial z}\right)+\frac{\gamma^2}{\chi}\frac{\partial}{\partial x}\left(\frac{1}{\chi}\frac{\partial u}{\partial x}\right)=u-(1-\xi)\bar{J}-\xi B \tag{A1}$$

we note two points: (*a*) The derivatives are to be evaluated along lines of constant x and of constant z. We thus introduce optical-depth increments $\Delta\tau_{i,j\pm1/2}\equiv|\tau(x_i,z_{j\pm1})-\tau(x_i,z_j)|$ and $\Delta\tau_{i\pm1/2,j}\equiv|\tau(x_{i\pm1},z_j)-\tau(x_i,z_j)|$. (*b*) The derivatives in the cross-derivative term do not commute.

A unique difference equation can be obtained if we represent the variation of u near (x_i, z_j) by a product of parabolic Lagrange interpolation polynomials in $\Delta\tau_x$ and $\Delta\tau_z$ on a nine-point stencil around the point under consideration. One finds

$$\begin{aligned}\frac{2\mu^2}{(\Delta\tau_{i,j-1/2}+\Delta\tau_{i,j+1/2})}&\left[\frac{u_{i,j+1}}{\Delta\tau_{i,j+1/2}}-u_{ij}\left(\frac{1}{\Delta\tau_{i,j+1/2}}+\frac{1}{\Delta\tau_{i,j-1/2}}\right)+\frac{u_{i,j-1}}{\Delta\tau_{i,j-1/2}}\right]\\&+\frac{2\gamma^2}{(\Delta\tau_{i-1/2,j}+\Delta\tau_{i+1/2,j})}\left[\frac{u_{i+1,j}}{\Delta\tau_{i+1/2,j}}-u_{ij}\left(\frac{1}{\Delta\tau_{i-1/2,j}}+\frac{1}{\Delta\tau_{i+1/2,j}}\right)+\frac{u_{i-1,j}}{\Delta\tau_{i-1/2,j}}\right]\\&-\mu\gamma\sum_{i'=i-1}^{i+1}\sum_{j'=j-1}^{j+1}(\alpha_{i'j}\beta_{i'j'}+\alpha_{i'j'}\beta_{ij'})u_{i'j'}=u_{ij}-(1-\xi_{ij})\bar{J}_{ij}-\xi_{ij}B_{ij}\,,\end{aligned} \tag{A2}$$

where

$$\alpha_{i\pm1,j'} \equiv \pm\Delta\tau_{i\mp1/2,j'}/[\Delta\tau_{i\pm1/2,j'}(\Delta\tau_{i-1/2,j'} + \Delta\tau_{i+1/2,j'})]\,, \tag{A3}$$

$$\alpha_{ij'} \equiv -(\alpha_{i+1,j'} + \alpha_{i-1,j'})\,, \tag{A4}$$

$$\beta_{i',j\pm1} \equiv \pm\Delta\tau_{i',j\mp1/2}/[\Delta\tau_{i',j\pm1/2}(\Delta\tau_{i',j-1/2} + \Delta\tau_{i',j+1/2})]\,, \tag{A5}$$

and

$$\beta_{i'j} \equiv -(\beta_{i'j-1} + \beta_{i',j+1})\,. \tag{A6}$$

Here $(i - 1 \le i' \le i + 1)$ and $(j - 1 \le j' \le j + 1)$.

In equation (A2) the terms of the form $(\alpha_{i'j}\beta_{i'j'}u_{i'j'})$ and $(\alpha_{i'j'}\beta_{ij'}u_{i'j'})$ represent $\{d[(du/d\tau_z)_j]/d\tau_x\}_i$ and $\{d[(du/d\tau_x)_i]/d\tau_z\}_j$, respectively. The elimination scheme used to solve the system is virtually identical to that described in the text except that $\boldsymbol{D}_{j,j\pm1}$ are void and $\boldsymbol{D}_{jj}$ is diagonal. One-sided differences are employed at exterior boundaries and corners.

APPENDIX B

EVALUATION OF OPTICAL DEPTH INCREMENTS

In a stellar atmosphere, the characteristic variation of χ is an exponential rise with depth, and a successful integration formula must address this fact. We assume that $\ln\chi$ is a piecewise linear function of the path-length s in the interval (s_0, s_1), i.e.,

$$\ln\chi = \ln\chi_0 + (\ln\chi_1 - \ln\chi_0)(s - s_0)/(s_1 - s_0) \equiv \ln\chi_0 + \beta(s - s_0)/\Delta s\,. \tag{B1}$$

Then

$$\Delta\tau = \int_{s_0}^{s_1}\chi ds = (\chi_1 - \chi_0)\Delta s/\beta\,, \tag{B2}$$

which is applicable if β is not too small. For $\beta \ll 1$, an economical approximation can be derived using the Euler-Maclaurin summation formula which yields

$$\int_{s_0}^{s_1}\chi ds \approx \tfrac{1}{2}\Delta s(\chi_1 + \chi_0) - \tfrac{1}{12}\Delta s^2(\chi_1' - \chi_0') + \Delta s^4(\chi_1''' - \chi_0''')/720\,. \tag{B3}$$

But $\chi' = (\beta/\Delta s)\chi$; hence

$$\Delta\tau = \tfrac{1}{2}\Delta s[\chi_1 + \chi_0 - \tfrac{1}{6}\beta(\chi_1 - \chi_0)(1 - \tfrac{1}{60}\beta^2)]\,, \tag{B4}$$

which is good to the accuracy of the computer word for $\beta \le 10^{-2}$.

REFERENCES

Ahlberg, J. H., Nilson, E. N., and Walsh, J. L. 1967, *The Theory of Splines and Their Applications* (New York: Academic Press).
Auer, L. H. 1976, *J. Quant. Spectrosc. Rad. Transf.*, **16**, 931.
Cannon, C. J. 1970, *Ap. J.*, **161**, 255.
Cannon, C. J., and Rees, D. E. 1971, *Ap. J.*, **169**, 157.
Carlson, B. G. 1963, in *Methods in Computational Physics*, Vol. **1**, ed. B. Alder, S. Fernbach, M. Rotenberg (New York: Academic Press), p. 1.
Cram, L. E., Durrant, C. J., and Kneer, F. 1977, *Report from the Workshop on Pluridimensional Radiative Transfer* (Naples: Osservatorio Astronomico di Capodimonte).
Feautrier, P. 1964, *C.R. Acad. Sci. Paris*, **258**, 3189.
Fox, L. 1962, *Numerical Solution of Ordinary and Partial Differential Equations* (Oxford: Pergamon Press), p. 216.
Hartree, D. R. 1958, *Numerical Analysis* (2d ed.; Oxford: Oxford University Press).
Jones, H. P. 1973, *Ap. J.*, **185**, 183.
Jones, H. P., and Skumanich, A. 1973, *Ap. J.*, **185**, 167.
———. 1977, in *Interpretation of Atmospheric Structure in the Presence of Inhomogeneities*, ed. C. J. Cannon. Report of IAU Commission 12, Grenoble (Sydney: University of Sydney Printing Office).
Kulander, J., and Jefferies, J. 1966, *Ap. J.*, **146**, 194.
Rybicki, G. 1971, *J. Quant. Spectrosc. Rad. Transf.*, **11**, 489.

L. Auer and D. Mihalas: High Altitude Observatory, National Center for Atmospheric Research, P.O. Box 3000, Boulder, CO 80307

Barbara Mihalas: Department of Astrogeophysics, University of Colorado, Boulder, CO 80309